Photocatalytic reduction of hexavalent chromium using Zn_2SnO_4–ZnO modified g-C_3N_4 composite

Damian C. Onwudiwe [b,a,*], Nombulelo Gobile [a,b], Opeyemi A. Oyewo [c], Seshibe S. Makgato [c]

[a] Department of Chemistry, School of Physical and Chemical Sciences, Faculty of Natural and Agricultural Sciences, North-West University, Mafikeng Campus, Private Bag X2046, Mmabatho, 2735, South Africa
[b] Material Science Innovation and Modelling (MaSIM) Research Focus Area, Faculty of Agriculture, Science and Technology, North-West University (Mafikeng Campus), Private Bag X2046, Mmabatho, South Africa
[c] Department of Chemical Engineering, College of Science, Engineering and Technology, University of South Africa, South Africa

ABSTRACT

In this study, a novel hierarchical g-C_3N_4/Zn_2SnO_4–ZnO heterojunction system was reported as an efficient photocatalyst for the reduction of Cr(VI). The fabrication of the composite involved the synthesis of the complex metal oxide (Zn_2SnO_4–ZnO), followed by the in-situ integration into graphitic carbon nitride. The structure, morphology, and optical properties of the as-prepared tertiary composite were determined using various analytical techniques. The results indicated the improvement in surface area and the electronic structure of the semiconductor heterostructures. Photocatalytic measurement showed the efficiency of the ternary composite to cause a reduction of the band gap energy, delayed charge recombination process and enhancement of the visible light absorption. Reaction parameters including the solution pH, photocatalyst (g-C_3N_4/ZTO-ZnO) dosage, and the initial concentration of Cr(VI) on the degradation efficiency of the photocatalyst were evaluated. The solution pH was varied from 2 to 8, and pH 2 displayed the highest removal of Cr(VI) with 99.2 % removal efficiency for the g-C_3N_4/ZTO-ZnO, while the ZTO-ZnO exhibited 72 % efficiency. Finally, the kinetic study of the photocatalytic reaction showed an increase in the overall rate constant *k* with the increase in initial concentration of Cr(VI). The outstanding performance of the ternary composite compared to the bare complex metal oxide makes the innovative g-C_3N_4/Zn_2SnO_4–ZnO composite a promising material for the removal of Cr(VI) from aquatic environment.

1. Introduction

Chromium is widely used in several industries, such as leather tanning, metal plating, steel manufacturing, as well as in pigment and refractory industries [1]. It is one of the heavy metals whose character ranges from an important trace metal to a deadly toxin. Its property depends on its oxidation state, and the most stable forms are +3 and + 6. Cr(III) is an essential nutrient that helps the body to utilize sugar protein and fat [2]. In this +3 oxidation state, it is relatively insoluble, poorly adsorbed into cell tissue, and does not bioaccumulate. Cr(VI), on the other hand, is mobile due to its solubility, simply absorbed into cell tissues, and can easily bioaccumulate in the human body where it is deadly [3]. Many countries have included Cr(VI) as one of the priority pollutants in their list of hazardous substances. This is due to its toxicity and carcinogenic properties known for several years [1,4]. The health

organs that are affected due to high exposure of Cr(VI) are the lungs, liver, and kidney. These organs play major roles in the functioning of the human body, therefore exposure to high concentrations of Cr(VI) could lead to death [5,6].

Various techniques have been used to treat Cr(VI) contamination, these include: ion exchange, electrocoagulation, membrane separation, adsorption, electrochemical precipitation, solvent extraction, evaporation, reverse osmosis and biosorption [7–9]. Despite the efficiency and progress achieved with these techniques, there are serious setbacks associated with them such as generation of sludge, production of secondary pollutants, high maintenance in terms of cost and low efficiency. These setbacks limit their real-life applications.

Since current conventional methods are not fully equipped to remove Cr(VI), there is ongoing research to explore more efficient, environmentally safe and cost effective methods of Cr(VI) removal from aqueous

systems [10]. Photocatalysis has emerged as a technique that utilizes sunlight to completely remove this heavy metal in wastewater without leaving traces of toxic by-products [11,12]. However, a few challenges associated with photocatalysis are slow reduction rate and poor reduction efficiency due to the recombination of electron-hole pair [11]. This problem could be addressed through the design of the right band alignment via the combination of two or more semiconductors to form a heterojunction [13]. Band alignment addresses fast electron hole recombination and helps alter absorption region from ultraviolet to visible region. This makes it a good candidate for more effective and efficient removal of Cr(VI) in wastewater.

Semiconductors are used as tools in photocatalysis because they have band gaps that promotes generation of electrons and holes. These excitons are responsible for the production of radicals that are used in the process of pollutant degradation. However, to utilize the process to its fullest capabilities the right semiconductor needs to be employed for the process through the right band gap alignment. The modification of traditional semiconductors by the formation of a heterojunction system results in the reduction of band gap energy and delay of recombination process. The former allows the nanoparticles to absorb more in the visible region, thereby improving its optical properties and enhancing its photocatalytic activities as well. The former increases the lifespan of the excitons, thus enhances its efficiency.

This research investigates the modification of traditional semiconductors through the formation of heterojunction system involving Zn_2SnO_4–ZnO nanoparticles. Zn_2SnO_4, also called the zinc stannate [14], is a typical ternary oxide semiconductor and belongs to the class of (II-IV-VI) oxides of the form $A_2^{II}B^{IV}O_4$. It is a transparent *n*-type semiconductor, and its band gap is around 3.6 eV, with a low absorption coefficient, and high chemical sensitivity. In addition, it is very stable under extreme conditions (very high temperatures) and possesses high electron mobility and conductivity ($\sim 10^4$ S cm^{-1}) [15]. Furthermore, it exhibits superior optical properties than its binary counterparts, and accounts for its extensive applications in solar cells, lithium batteries, sensors including the degradation of organic pollutants in wastewater [14].

Zinc stannate is found in two dissimilar crystallographic structures: the $ZnSnO_3$, which has an orthorhombic phase and Zn_2SnO_4 of cubic phase. The metastable perovskite ($ZnSnO_3$) form is produced at a temperature ranging from 350 to 750 °C. At higher temperature > 750 °C, it is then transformed to the stable cubic spinel (Zn_2SnO_4) structure [16]. The cubic phase Zn_2SnO_4 is a face-exposed octahedron, while orthorhombic $ZnSnO_3$ is a face-exposed hexahedron structure [17]. The metastable $ZnSnO_3$ has crystal lattice with two cation sites, where the Sn^{4+} is located at the corners, while Zn^{2+} is found in the centre together with the oxygen anion. Furthermore, the structure has strong covalent bonds between zinc and oxygen atoms and is said to be non-centrosymmetric [18]. Several $ZnSnO_3$ structures have been reported with space group (R-3) and lattice parameters a = 5.2835 Å, c = 14.0913 Å [19–21]. In Zn_2SnO_4, its (O^{2-}) anions are organized in a rather cubic lattice with Sn^{2+} and Zn^{2+} cations located at some or all tetrahedral and octahedral sites. The lattice parameter of Zn_2SnO_4 is a = 8.65 Å with space group of Fd3m [14].

Numerous studies have reported on the application of zinc stannate as a photocatalyst [22–24]. Most reports on the photocatalytic activity are within the UV light because of the optical absorption of zinc stannate, which lies in the UV region. Zn_2SnO_4 nanowires have been reported to exhibit a blue-green emission at around 400–600 nm under UV light, revealing that Zn_2SnO_4 has exceptional potential in the field of photovoltaic devices and photocatalysis [25]. The photocatalytic properties of the different structures of Zn_2SnO_4 have been evaluated using Congo red as a model contaminant [26], and both the size and morphology of the particles were found to influence the photocatalytic activity. The study from the photoluminescence measurements found that the influence in photocatalytic activity could be attributed to enhanced oxygen vacancies and crystallite defects formed by

substitution of Zn^{+2} in the lattice of SnO_2. Recently, Zn_2SnO_4 was prepared using the microwave assisted method and the photocatalytic activity was evaluated [27]. Studies have been expanded further to investigate the composites of zinc stannate with other compounds like the carbon-based materials including graphene oxide and graphitic carbon nitride, and how different combinations enhance its application in the field of photocatalysis [28,29].

Graphitic carbon nitride is a polymeric semiconductor that consists of two units, tri-*s*-triazine (C_6N_7) and s-triazine (C_3N_3). It is capable of emitting light in the visible region at approximately 400–475 nm. Luminescent g-C_3N_4 show excellent optical properties, including adjustable emission wavelength, no light scintillation and a stable fluorescence signal [30]. When the surface of g-C_3N_4 is modified or doped with other materials, the fluorescence emission quantum yield is comparable to the high-performance semiconductor quantum dots, but at the same time safer as it does not affect the action of the biomolecules. Due to its ability to harvest solar energy, g-C_3N_4 is capable of being used as a photocatalyst and its use in different areas of photocatalysis has been extensively reported. One of the first possible use of g-C_3N_4 as a photocatalyst was reported by Wang et al. [31], after which the research on g-C_3N_4 as photocatalyst expanded. However, the sue of pristine g-C_3N_4 in photocatalysis suffers some disadvantages such as low surface area, high charge recombination, and limited visible light absorption [32].

Both ZTO and g-C_3N_4 n-type semiconductor with wide bandgaps, so forming a heterojunction using the two semiconductors results in a narrow bandgap. Furthermore, incorporating the ZTO into g-C_3N_4 will result in the construction of heterojunction of the type II band alignment, thereby enhancing its photocatalytic activity compared to the pristine g-C_3N_4 or ZTO [33–35]. This type of system would have enhanced activity due to the reduction of the recombination processes, and would be effective in addressing some environmental challenges such as the photoreduction of Cr(VI) to Cr(III) [32].

Here, a composite of zinc stannate and zinc oxide nanoparticles were prepared and were subsequently incorporated into graphitic carbon nitride at different ratios using high temperature solid state method. The nanocomposites were then used for the reduction of Cr(VI) to Cr(III) in water.

2. Experimental

2.1. Materials and methods

The metal salts: tin(II) chloride dihydrate and zinc acetate dihydrate; and the reagents for the synthesis of the dithiocarbamate ligands: N-methylaniline, carbon disulphide, ammonium hydroxide, and ethanol were obtained from Merck chemicals and were used as received.

2.2. Synthesis of zinc stannate-zinc oxide (ZTO-ZnO) nanoparticles

Zn(II) bis(*N*-methyl-*N*-phenyldithiocarbamate) (0.5 g), which was prepared following an earlier reported procedure [36], was sonicated in ethanol for 5 min. This was followed by the introduction of different percentage ratios (2, 5, 10, 15 and 20 %) of tin(II) chloride dihydrate solution. After thorough stirring for 20 min, the suspension was then transferred into an autoclave and heated for 4 h at 70–80 °C. The product was centrifuged, washed thoroughly with water and ethanol to remove any impurities, and was air dried at room temperature overnight. The dried sample was calcined at 1000 °C for 4 h to afford Zn_2SnO_4–ZnO.

2.3. Synthesis of g-C_3N_4/ZTO-ZnO nanocomposite

The g-C_3N_4/ZTO-ZnO nanocomposite was prepared by mixing melamine and ZTO-ZnO in ratio 2:1 (wt/wt) using mortar and pestle. Then, the blend was transferred into a crucible and calcined for 4 h at 600 °C.

The resulting product was left to cool to room temperature then collected for analysis.

2.4. Characterization of the prepared samples

UV–vis measurements were carried out using Varian UV–vis spectrophotometer. Photoluminescence (PL) spectra were recorded on a PerkinElmer LS 45 Fluorimeter. Diffraction patterns of the samples were obtained on Bruker D8 Advanced XRD instrument, and the patterns obtained were compared to the standard JCPDS database. The morphology of the samples was analyzed using a JEOL 6400F Field Emission SEM at 5 kV and Hitachi HF–2000 TEM at 200 kV.

2.5. Photocatalytic degradation of Cr(VI) in water

The degradation of Cr(VI) in dichromate ions solution were investigated using both nanocomposites under the visible light irradiation. A circulating water source in the reactor vessel with a 250–W Xe discharge lamp was used for this study. About 0.5 mg/L concentration of the dichromate ion, and 0.5–2.0 mg of the nanocomposites were varied in this study. The photocatalyst was introduced into the dichromate ion solution and stirred magnetically in the dark for 1 h until the adsorption equilibrium was reached. The suspension was then exposed to the lamp for 2 h with continuous stirring. The aliquots were taken from the solution at 15, 30, 45, 60, 90 and 120 min intervals. The degradation efficiency of the dichromate ion was studied using UV–visible spectrophotometer.

2.6. Calculation of the percentage degradation of Cr(VI)

The percentage of the photocatalytic degradation of dichromate ion was calculated using the following equation:
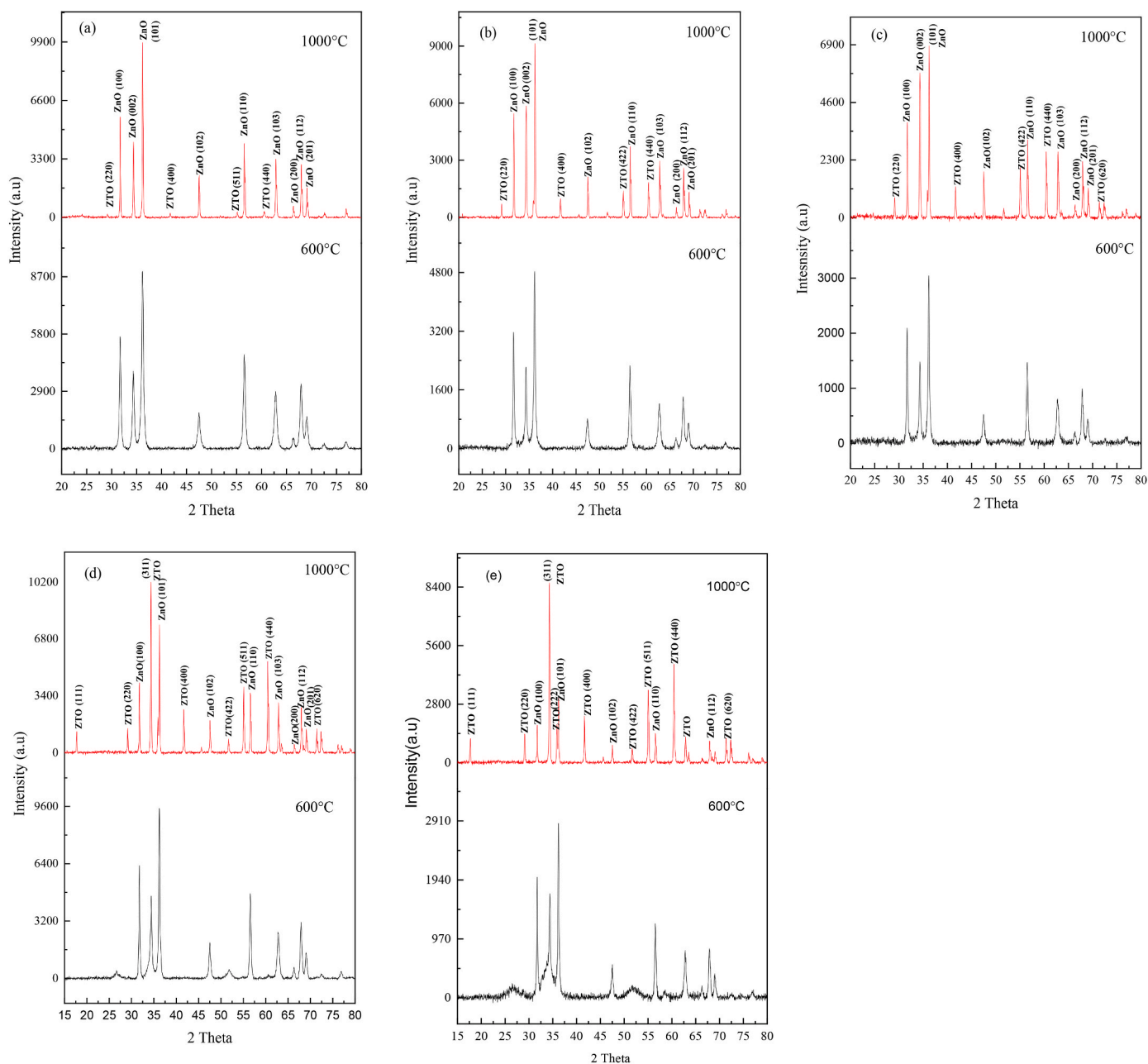

Fig. 1. Overlaid XRD patterns of the ZTO-ZnO prepared at different temperatures (600 and 1000 °C) using a 0.5 g of Zn(II) dithiocarbamate and (a) 2, (b) 5, (c) 10, (d) 15, and (e) 20 % SnCl$_2$.

Degradation yield $\% = \frac{C_o - C_e}{C_o} X\ 100$ (1)

where, C_0 is the initial concentration C_e is the concentration of dye after degradation.

3. Results and discussion

3.1. X-ray diffraction (XRD) studies

Reaction temperature played a critical role in the samples' crystallinity and products obtained from the calcination process. At 600 °C and generally below 1000 °C, the zinc stannate peaks were not identified in the diffraction patterns even at the different percentage concentration. However, an increase in the calcination temperature to 1000 °C, resulted in the emergence of a peaks at 2θ = 17.9, 29, 34.4, 35.9, 41.8, 51.8, 55, and 60.4, which were ascribed to the (111), (220), (311), (222), (400), (422), (511) and (440) diffraction patterns of zinc tin oxide (ZTO). This was consistent with the standard JCPDS card No: (00-0 24-1470) and corresponded to the face-centred cubic structure of ZTO with lattice constant a = 8.65740 [37]. The formation of zinc stannate peak at such a very high temperature could be due to the formation of SnO_4 from the $SnCl_2$ and subsequent reaction of this oxidised form of Sn with the ZnO (obtained at 600 °C), thereby resulting in Zn_2SnO_4–ZnO.

Fig. 1(a–e) present the overlapped XRD patterns for the samples prepared at 600 and 1000 °C using 2, 5, 10, 15 and 20 % (wt/wt) $SnCl_2$ respectively. It could be observed that only ZnO was clearly observable at 600 °C and ZTO became more conspicuous as the concentration of Sn was increased, which was clearly evident in Fig. 1e. The samples obtained at 1000 °C showed improved crystallinity compared to those at 600 °C, therefore confirming that temperature has a good effect on crystallinity.

Scherrer's and Williamson Hall's methods were used for the crystallite size estimation of the samples. As a simplified integral breadth method, Williamson Hall method considers the peak width of the diffraction patterns as a function of 2θ. Hence, it deconvolutes both the size and strain induced broadening [9]. The calculated crystallite sizes from both methods are presented in Table 1, including other geometric parameters obtained from the Williamson Hall's method.

The formation of heterojunction systems and the high temperature synthesis condition influenced both the crystalline structure and geometrical parameters of the samples. Table 2 summarises the lattice properties of the ZTO-ZnO at 1000 °C. Only slight changes in the lattice parameters occurred with variation in the amount of $SnCl_2$ added to the system. This implies that no significant change in lattice parameters could take place without a structural change, and very slight change in the amount of precursor concentration may not be sufficient to induce any strain/stress within the crystalline lattice.

The ZTO-ZnO(20) nanoparticles was incorporated into g-C_3N_4 to form a ternary heterojunction nanocomposite. Fig. 2a presents the

Table 1
The geometric parameters of ZTO-ZnO nanoparticles prepared at 1000 °C for different concentrations of $SnCl_2$.

Sample	% of SnCl₂ added	Scherer Method	Williamson- Hall method	
	(%)	D nm	D nm	ε x 10^{-3}
ZnO	2	35.6	93.1	1.22
ZTO(2)		81.0	41.11	108.23
ZnO	5	36.2	106.7	1.28
ZTO(5)		60.0	47.8	10.95
ZnO	10	37.1	88.9	1,14
ZTO(10)		55.5	64.2	2.88
ZnO	15	39.5	86,2	1.07
ZTO(15)		57,4	105.1	1.58
ZnO	20	41.1	18,3	3,08
ZTO(20)		51.9	90.6	2.7

Table 2
The structural parameters of ZTO-ZnO nanoparticles prepared at 1000 °C for different concentrations of $SnCl_2$.

Sample	2θ	Hkl	Dhkl (Å)	Structure	Lattice Parameter (Å)	V(Å³)
ZTO-ZnO (2)	34.38	311	2.6079	Face centred cubic	a = 8.6497	647.1472
ZTO-ZnO (5)	34.39	311	2.6076	Face centred cubic	a = 8.6482	646.8173
ZTO-ZnO (10)	34.32	311	2.6130	Face centred cubic	a = 8.6664	650.9028
ZTO-ZnO (15)	34.35	311	2.6105	Face centred cubic	a = 8.6581	649.0322
ZTO-ZnO (20)	34.32	311	2.6130	Face centred cubic	a = 8.6664	650.9028

overlaid diffraction patterns of the pristine graphitic carbon nitride, the binary nanocomposite, and the ternary heterojunction nanocomposite. The diffraction pattern of the g-C_3N_4 exhibited a peak around 28 °C corresponding to (002) plane of g-C_3N_4 (JCPDS 00-087–1526) [38,39]. The (0 0 2) plane is a characteristic interplanar stacking peaks of aromatic systems. The XRD patterns of ZTO-ZnO showed characteristic peaks which could be indexed to the (111), (220), (311), (222), (400), (422), (511), (440), (531), (533) and (622) plane of cubic structure, with lattice constant a = 8.65740 Å [40]. The obtained data is consistent with (JCPDS: 00-024-1470) [14]. Other diffraction peaks could be assigned to hexagonal phase with Wurtzite structure, space group ($P6_3mc$) (186), JCPDS card No.36–1451 and unit cell parameters a = b = 3.249823 Å and c = 5.20661 Å confirming no change in the crystallinity of the ZnO even in the ternary system. In addition, the presence of all the peaks from the precursor components ZTO-ZnO and g-C_3N_4, confirmed the successful incorporation of ZTO-ZnO nanoparticles into the g-C_3N_4 by both approaches devised. For comparison, Fig. 2a presents the diffraction patterns of pristine g-C_3N_4, ZTO-ZnO(20), and g-C_3N_4/ZTO-ZnO (20) nanocomposite. There was no additional phase identified, which confirmed the purity of the synthesized samples.

The compositing of the g-C_3N_4 with nanoparticles could alter its polymeric nature, resulting to a shift in the characteristic (002) plane towards the lower 2θ position as observed in the overlaid patterns in the lower angle shown in Fig. 2b. This could be attributed to a successful incorporation of the complex metal oxide into g-C_3N_4, located in the in-plane holes of carbon nitride (bound to the nitrogen atoms) [41].

3.2. Proposed pathway for the synthesis of ZTO-ZnO nanoparticles

A synthesis pathway has been proposed for the successful synthesis of the binary complex oxide nanoparticles from the Zn(II) dithiocarbamate complex and $SnCl_2$ as precursors. The utilisation of metal dithiocarbamate complexes as single source precursors relies on the volatility of the metal complexes, the strength of the metal–sulphur and carbon–sulphur bonds. The thermal decomposition of some M(II) (Ni and Zn) and M(III) (Cr and Co) complexes of *N*-methylbenzyl– and 4-morpholine–DTC complexes, were reported as early as 1974 [42]. The complexes decomposed to their respective metal sulphides with the loss of H_2S, and the formation of isothiocyanate as intermediate product [43]. Recent studies have confirmed this as a general trend amongst most dithiocarbamate complexes [44]. However, these are based on observation deduced from experiment conducted under inert atmosphere without the possibility of oxidation.

Based on the calcination products and supported by the reported decomposition pathways of metal dithiocarbamates, studied with the aid of GC-MS [43,45], a schematic representation of decomposition
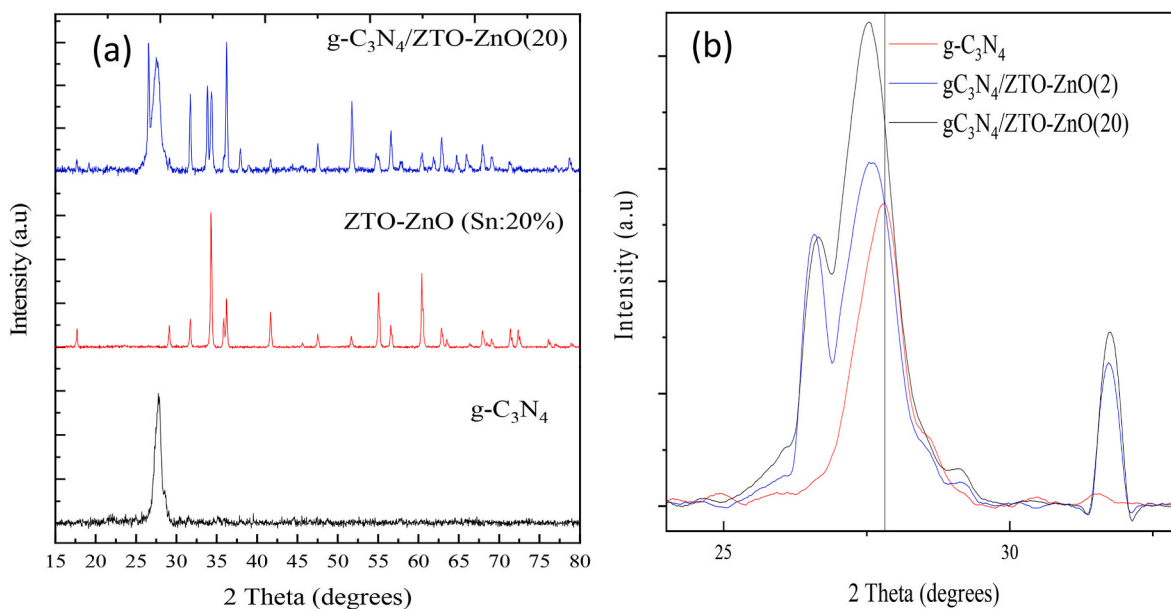
Fig. 2. X-ray diffraction patterns of (a) pristine g-C$_3$N$_4$, ZTO-ZnO(20), and g-C$_3$N$_4$/ZTO-ZnO(20) nanocomposite, (b) enlarged view of peaks in the lower 2 theta values for the X-ray diffraction patterns of pure g-C$_3$N$_4$, and g-C$_3$N$_4$/ZTO-ZnO.

profile leading to ZnO has been proposed and presented in Scheme 1. The first decomposition step was the homolytic dissociation of [Zn(S$_2$CNMePh)] into Zn(S$_2$CNMePh) and S$_2$CNMePh radicals. Although, the possibility of a heterolytic dissociation exists, the homolytic scission of the metal–sulphur bond to generate dithiocarbamate radicals is significantly more favourable than heterolytic scission. About 143 kJ mol^{-1} energy was required for the former and 678 kJ mol^{-1} for the later in an experiment conducted using [Cu(S$_2$CNEt$_2$)$_2$] [46–48].

Therefore, with similar [Zn(S$_2$CNMePh)], a possible slightly lower enthalpy is expected for a homolytic dissociation. After this first decomposition, there are possible pathways for the second step: (a) the dissociation of the second dithiocarbamate radical via an intramolecular rearrangement (a′) to form ZnS moieties and the loss of thiocyanide and an alkyl group (Me); (b) the dimerization of the resulting Zn(S$_2$CNMePh) and S$_2$CNMePh radicals (from the homolytic cleavage) to form a thiuram moiety accompanied with the formation of Zn metal. It is hard to distinguish between these processes. However, considering that zinc has no redox chemistry and, therefore, cannot undergo an intramolecular oxidative-addition, it is expected that the homolytic loss of the second dithiocarbamate radical would have an energy barrier very similar to the first dithiocarbamate loss. A free-radical decomposition mechanism has been supported by an investigation by Wold et al. [49], via studying the organic components of the decomposition of [Zn(S$_2$CNEt$_2$)$_2$] at 450 °C using mass spectrometry. In the reaction, EtNCS, Et$_2$NH, CS$_2$, and ethylene were identified as products.

In the presence of oxygen (such as the current study conducted in open air), pathway (c) showed that oxidation of the Zn metal could take place, resulting in the formation of ZnO. The introduction of Sn(II) led to the formation of Sn within the lattices of the ZnO, hence resulting in Sn doped ZnO at 600 °C (path d) as confirmed by the XRD patterns. However, as the temperature increased, oxidation of Sn to SnO$_2$ occurred, followed by the reaction of the SnO$_2$ with the ZnO to form a stannate. This last step was strongly dependent on the concentration of the of the SnCl$_2$ in the starting reagent.

Crystal defects in semiconductor nanoparticles permit the excitation of electrons from the valence band to the conduction band. Surface and core defects in nanoparticles are of great importance for photocatalysis reactions. The defect states in the nanocrystals activate visible light photocatalysis in metal oxide semiconductors [50]. The calcination process involved in the synthesis of the Sn doped ZnO lead to the crystal defects and the formation of ZTO-ZnO.

3.3. Morphological studies

The SEM images of the prepared composites are shown in Figs. 3 and 4. The images illustrate the occurrence of particles in two different morphologies. Fig. 3 presents the results of ZTO-ZnO(2), ZTO-ZnO(10), and ZTO-ZnO(10) composite oxides. The images show the admixture of cubic and rectangular particles for ZTO-ZnO(2) and ZTO-ZnO(10). Compact arrangement of particles with spherical morphology and no distinct separable edge were observed in ZTO-ZnO(10). The ZTO-ZnO (15) and ZTO-ZnO(20) composites shows the emergence of more cubic and granular particles (Fig. 5). The granular particles could possibly be ZnO nanogranules, while the rectangular shaped particles could be ZTO particles.

During the synthesis of ZTO, Zn^{2+} ions from the ZnO surfaces reacted with Sn^{2+} ions available in the precursor solution forming ZTO compounds [51]. The morphology of the composite formed could be seen to be influenced by the concentration of the precursor (SnCl$_2$) used. At low concentration of Sn ion, the possible amount of ZTO formed were low. When higher concentration of a Sn ion was used for the synthesis of the nanocomposite, more of the ZnO were transformed to the nanocomposite with ZTO. Furthermore, a change in morphology was also observed with the dominance of nanoparticles with cubic morphology. This was due to the higher concentration of Sn^{2+} in the solution, which resulted in increased consumption of Zn^{2+} ions released from ZnO, exposing the surfaces to the Sn^{2+} solution to further form ZTO [3]. Hence, may account for the increase in non-uniform cubic ZTO nanoparticles.

TEM images of the binary ZTO-ZnO nanocomposite are presented in Fig. 5(a–e), and presents two different morphologies that complement the SEM results of the nanoparticles. The two morphologies identified are the rectangular shaped particles for the ZTO-ZnO:Sn(2) (Fig. 5a), which tend to decompose into an admixture of cubic and spherical morphologies (Fig. 5 b-e) as the concentration of the Sn^{2+} ion increases. The ZTO were formed by the reaction of the ZnO and SnO$_2$, with the dissolution of the crystalline structure and its subsequent re-precipitation in the system wherein Sn^{2+} ion in the solution reacts with Zn^{2+} supplied from ZnO nanospheres forming ZTO [51,52].

In the HRTEM images, distinct lattice fringes confirming the
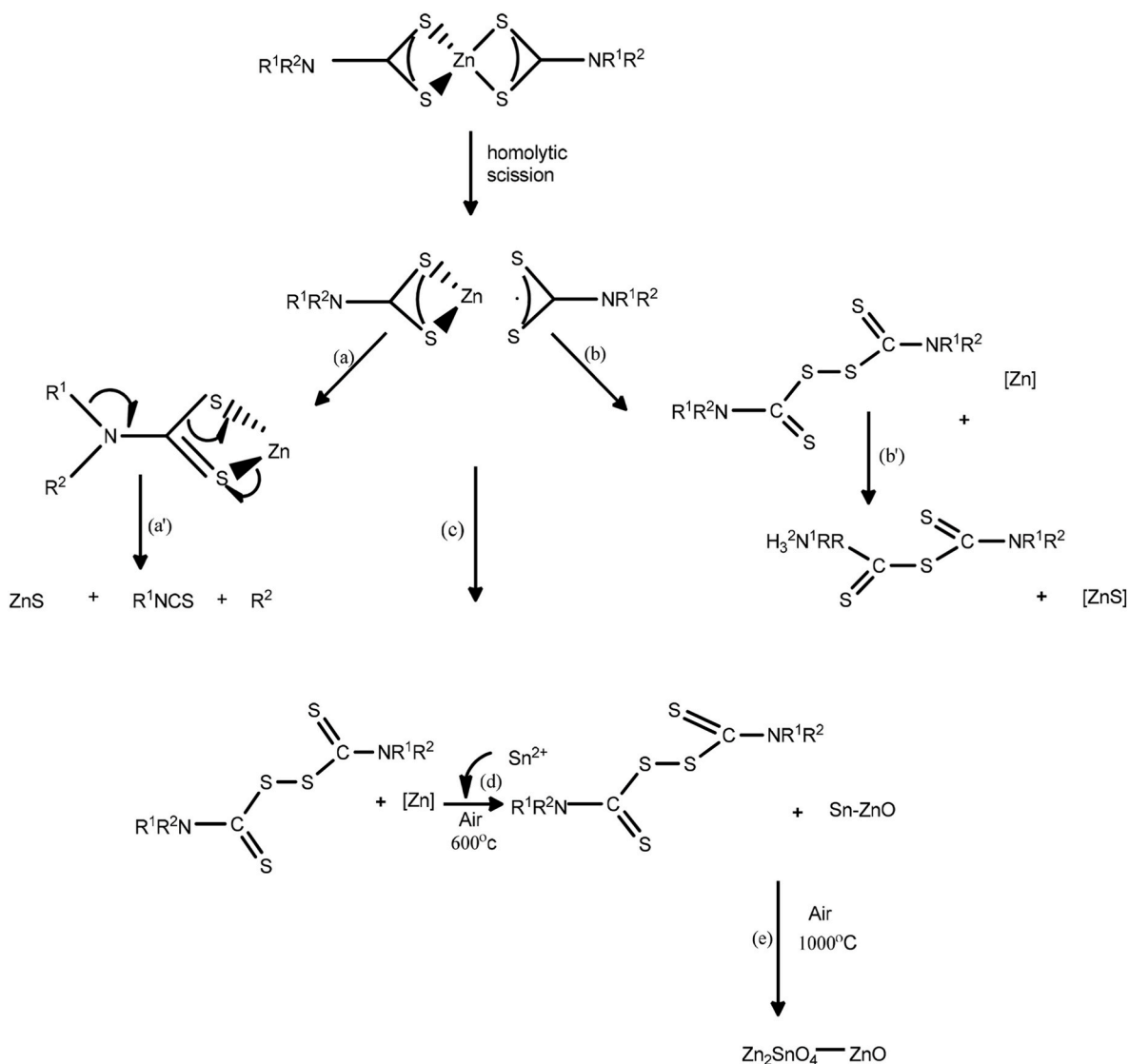
Scheme 1. Schematic representation of possible decomposition mechanism of the Zn(II) dithiocarbamate complex in air and the formation of the zinc stannate in the presence of SnCl$_2$.

crystallinity of the particles are evident (Fig. 5 f). The lattice fringes of ZTO-ZnO, with inter-planer distance of 0.50 nm, corresponding well with the (1 1 1) planes, and 0.28 nm which corresponds to the (1 0 0) planes of hexagonal ZnO, as shown (Fig. 5 (g)) further confirm the presence of Zn$_2$SnO$_4$ and ZnO phases in the composite. This is supported by the EDX spectrum of Fig. 5 h. These results confirm the results obtained from XRD studies and the existence of mixed ZnO and ZTO phases in the same system.

The SEM image of the g-C$_3$N$_4$ in Fig. 6a are composed of many irregular nanosheets, which are the characteristic of g-C$_3$N$_4$ [53–55]. The SEM images of g-C$_3$N$_4$/ZTO-ZnO (Fig. 6(b–f) confirmed the co-existence of g-C$_3$N$_4$ nanosheets and ZTO-ZnO nanocubes. The ZTO-ZnO nanocubes were deposited on the surface of the g-C$_3$N$_4$, indicating the formation of ternary g-C$_3$N$_4$/ZTO-ZnO composites [54]. A relatively rough surface could be observed on the g-C$_3$N$_4$ after the incorporation of ZTO-ZnO. The representative elemental mapping studies of the synthesized g-C$_3$N$_4$/ZTO-ZnO composites showed the C, N, O, Zn, and Sn elements are uniformly and evenly distributed (Fig. 7).

The TEM image of pure g-C$_3$N$_4$ in Fig. 8 (a) consists of nanosheets, which are characteristic of gC$_3$N$_4$ [56,57]. Fig. 8 (b - f) clearly reveal the differences in the morphology of the materials with introduction of the different concentrations of binary complex metal oxide. The ternary

heterostructure consists of g-C$_3$N$_4$ nanosheets decorated with very small particles of ZTO-ZnO [57].

3.4. Absorption properties of the ZTO-ZnO heterojunction systems

The absorption spectra of the ZTO-ZnO are shown in Fig. 9. An increase in the concentration of the SnCl$_2$ resulted in a red shift, which could be attributed to the increase in the rate of formation of electron–hole pairs on the semiconductor surface [58], resulting in higher photochemical activity. Table 3 presents the band gap energies of the different samples with variation in the concentration of SnCl$_2$ ion, which followed a decreasing trend from ZTO-ZnO(2 %) to ZTO-ZnO(20 %)

Optical absorption spectra of pure g-C$_3$N$_4$, and g-C$_3$N$_4$/ZTO-ZnO(20) are shown in Fig. 10. The pristine g-C$_3$N$_4$ showed a maximum absorption peak at 320 nm, while the g-C$_3$N$_4$/ZTO-ZnO(20) nanocomposites showed a decrease in the intensity of the maximum peak at 320 nm upon the introduction of g-C$_3$N$_4$. This is attributed to the interaction between g-C$_3$N$_4$ and ZTO-ZnO in the composites. The band gap of the g-C$_3$N$_4$, and g-C$_3$N$_4$/ZTO-ZnO(20) were estimated from the intercept of the tangents to the plots of $(\alpha h\nu)^2$ vs photoenergy (Fig. 10) as 2.7, and 2.06 eV respectively, suggesting that the band gap could be significantly narrowed by the introduction of a binary heterojunction into g-C$_3$N$_4$
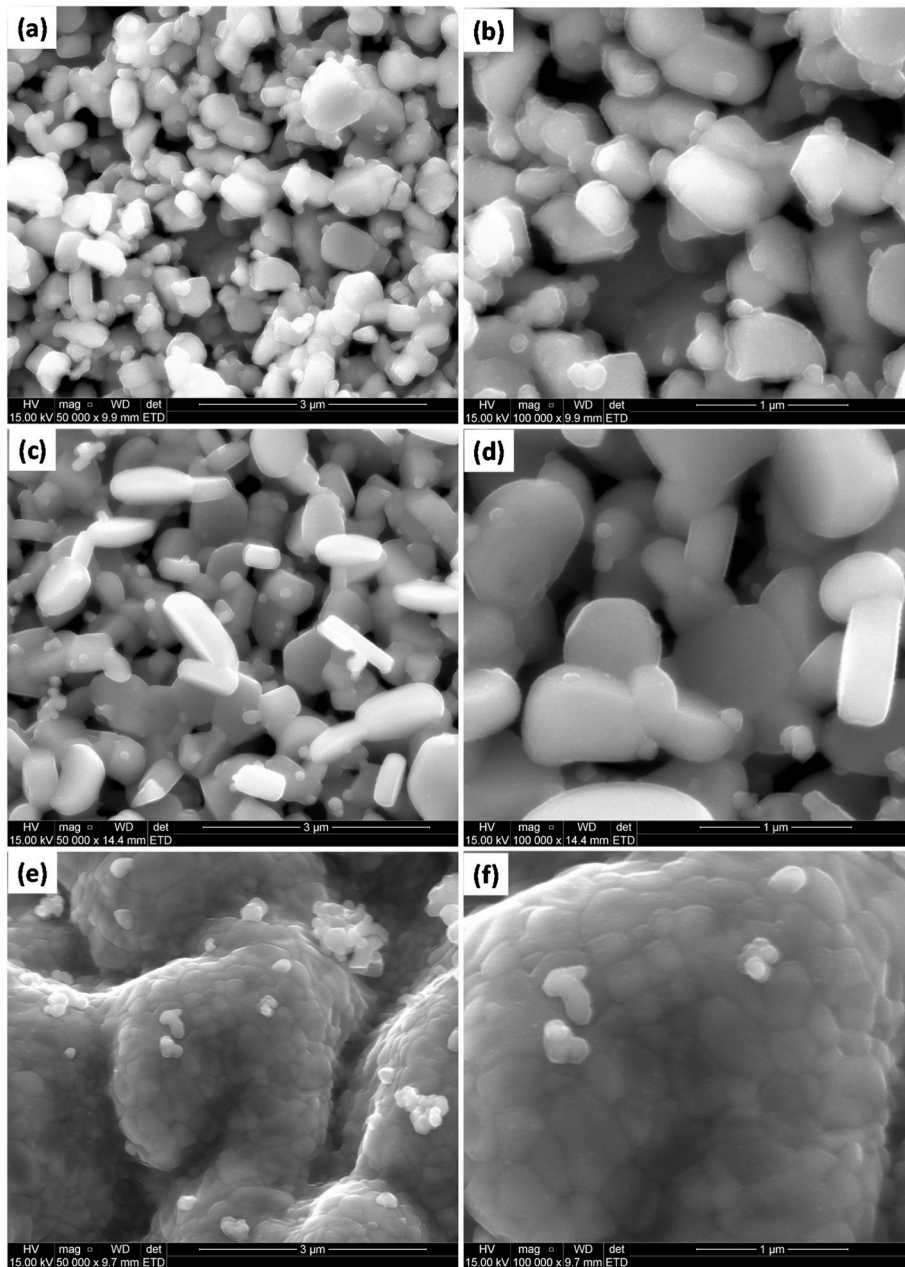
Fig. 3. SEM micrograph (a, b) ZTO-ZnO:Sn(2), (c,d) ZTO-ZnO:Sn(5) (e,f) ZTO-ZnO:Sn(10) at low and high magnification respectively.

interlayers [59].

3.5. Determination of valence band and conduction band edge

Both the conduction and valence band potentials (E_{CB}) and (E_{VB}) of the nanoparticles were determined using Mulliken electronegativity and the bandgap of a semiconductor given in Equations (2) and (3) respectively.

$$\mathbf{E}_{CB} = \boldsymbol{\chi} - \mathbf{E_e} - \mathbf{0.5E_g} \tag{2}$$

$$\mathbf{E}_{VB} = \mathbf{E}_{CB} + \mathbf{E_g} \tag{3}$$

E_e represents the energy of free electrons as measured on the hydrogen scale (4.5 eV) [60], while χ denotes the electronegativity of the nanoparticles. This electronegativity value is determined based on the geometric mean of all the constituent elements within the semiconductor nanoparticles. The electronegativity of the semiconductor

nanoparticle is determined from Equation (4).

$$\chi_{dDeEfFgG} = \left(\boldsymbol{\chi}\,(\boldsymbol{D})^d + \boldsymbol{\chi}(\boldsymbol{E})^e + \boldsymbol{\chi}(\boldsymbol{F})^f + \boldsymbol{\chi}(\boldsymbol{G})^g\right)^{(d+e+f+g)^{-1}} \tag{4}$$

where D, E, F and G are the elemental composition of the semiconductor and d, e, f, and g denote the number of atoms respectively.

The electron affinity and first ionization energy of the atoms are used to compute the Mulliken electronegativity of each atom in the semiconductor nanoparticles such that the electronegativity of atoms ($\chi(\boldsymbol{D}), \chi(\boldsymbol{E}), \chi(\boldsymbol{F}) and \chi(\boldsymbol{G})$) is estimated via Equation (5).

$$\chi_{element} = \frac{(\textbf{First ionization energy}\ (eV) + \textbf{Electron affinity}\ (eV))}{\mathbf{2}} \tag{5}$$

where $\chi_{element}$ is the Mulliken's electronegativity of the element in eV. Table 4 presents Mulliken's electronegativity of the nanoparticles, calculated from the First ionization energy and Electron affinity of the constituent atoms. The variation in the conduction band and valence
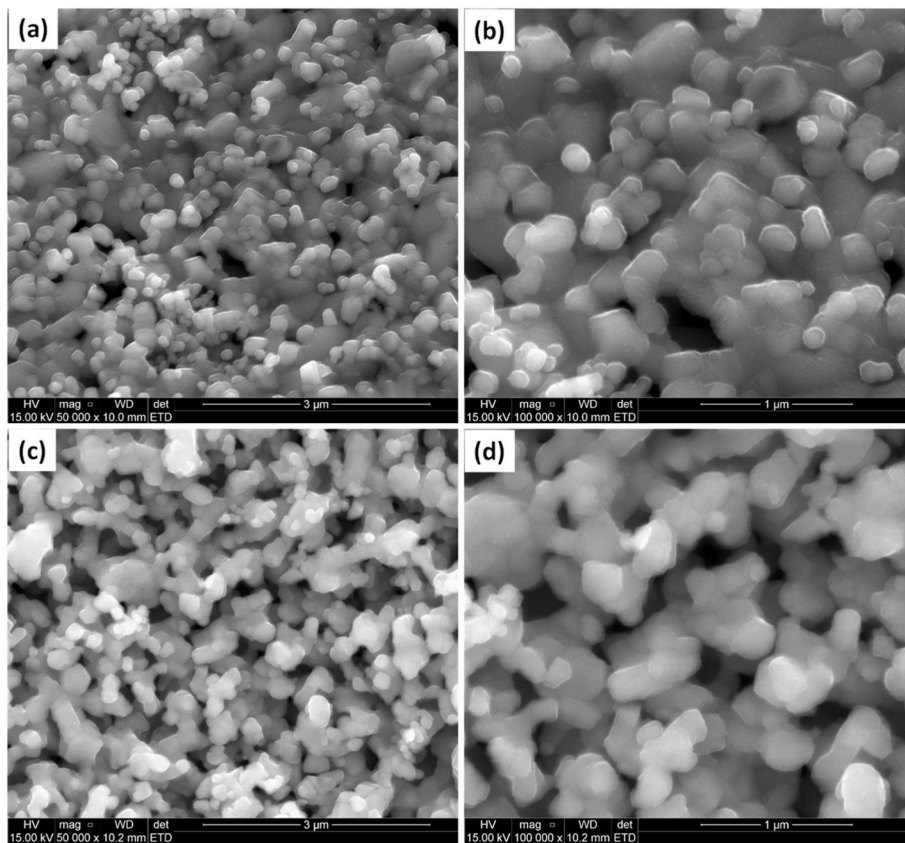
Fig. 4. SEM micrographs (a,b) ZTO-ZnO:Sn(15), and (c,d) ZTO-ZnO:Sn(20) at low and high magnification respectively.
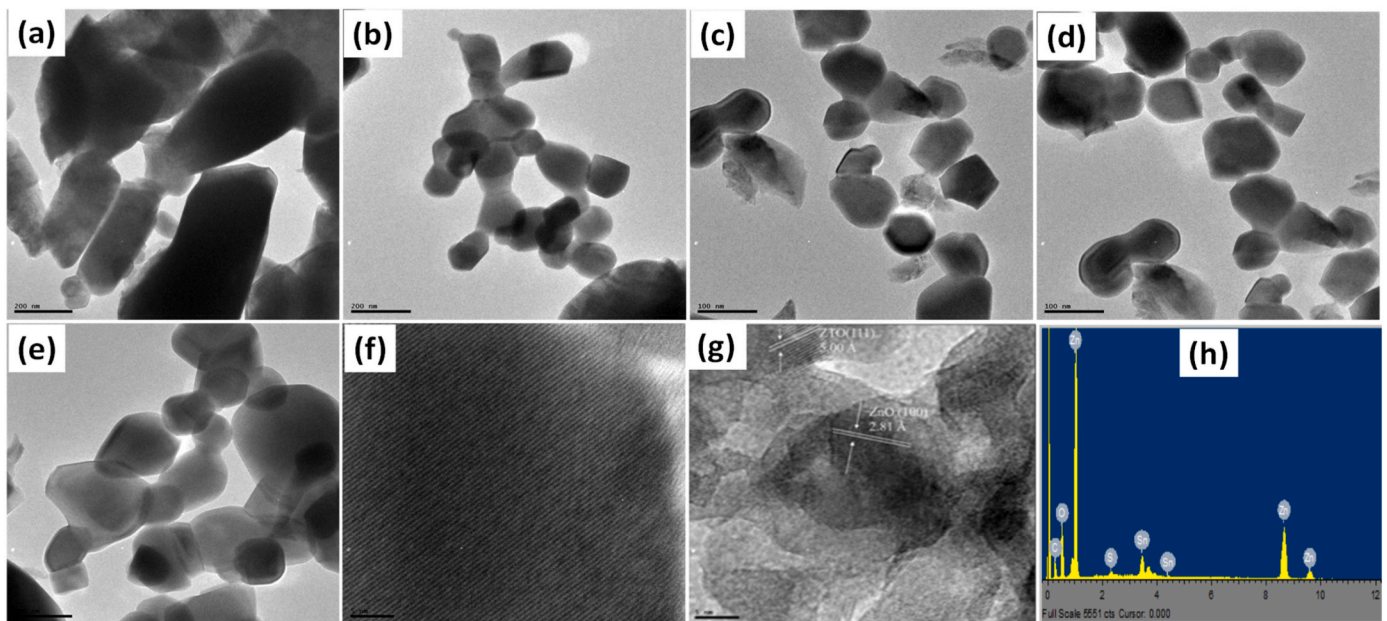

Fig. 5. TEM micrograph (a) ZTO-ZnO:Sn(2), (b) ZTO-ZnO:Sn(5), (c) ZTO-ZnO:Sn(10), (d) ZTO-ZnO:Sn(15), (e) ZTO-ZnO:Sn(20), and representative HRTEM of ZTO-ZnO showing distinct fringes and inter-planer distance for ZTO and ZnO. (h) The EDX spectrum for the ZTO-ZnO.

band of the pristine graphitic carbon nitride and the nanocomposite are shown summerized in Table 5.

3.6. Band structure and charge transport process in the ternary g-C₃N₂/ZTO-ZnO heterojunction system

A plausible mechanism for the photocatalytic reduction of hexavalent chromium by the g-C₃N₂/ZTO-ZnO was proposed based on the results obtained in 3.5 and is shown in Fig. 11. Upon the irradiation of
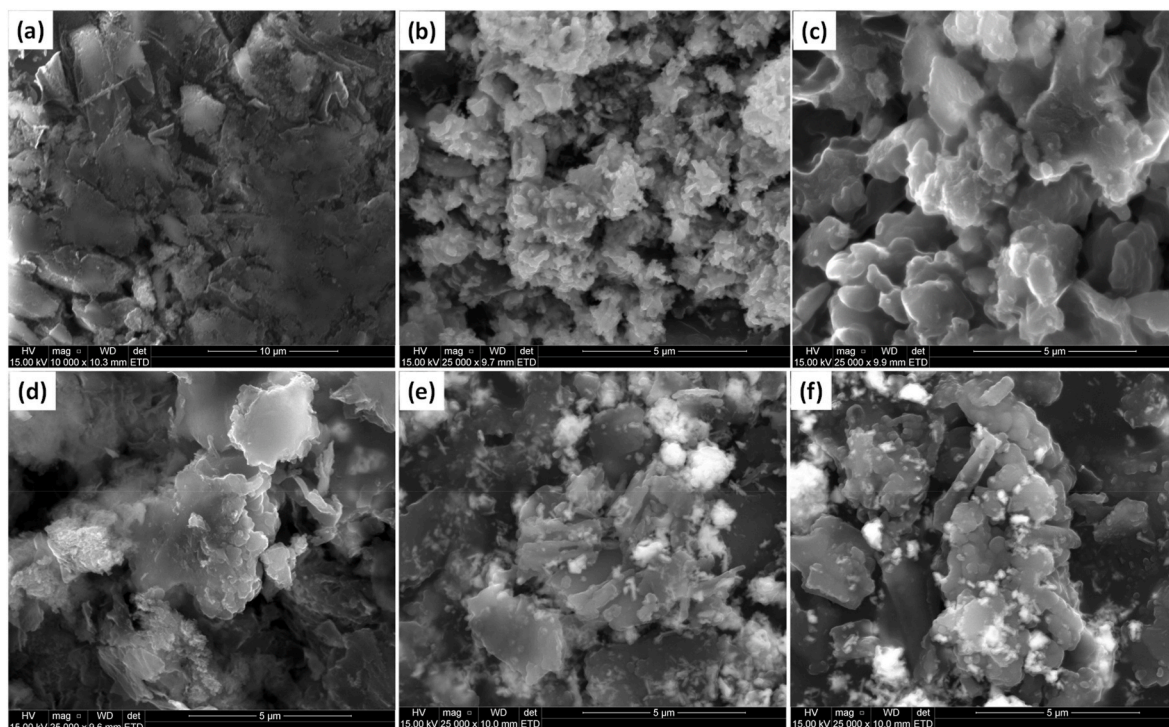
Fig. 6. SEM micrographs of (a) gC$_3$N$_4$, (b) gC$_3$N$_4$/ZTO-ZnO(2), (c) gC$_3$N$_4$/ZTO-ZnO(5), (d) gC$_3$N$_4$/ZTO-ZnO(10), (e) gC3N4/ZTO-ZnO(15), and (f) gC$_3$N$_4$/ZTO-ZnO(20).
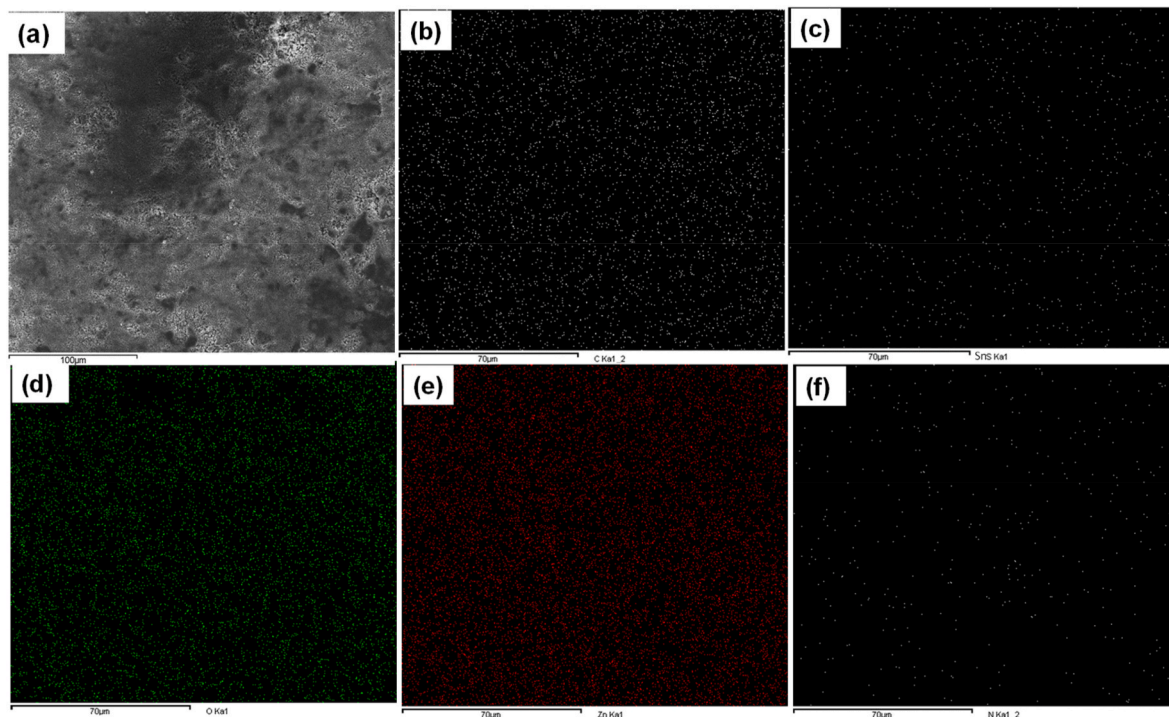

Fig. 7. (a) Elemental mapping of gC$_3$N$_4$/ZTO-ZnO(20) showing (b) C, (c) Sn, (e) O, (e) Zn, and (f) N.

the ternary nanocomposite system (g-C$_3$N$_2$/ZTO-ZnO) with visible light, excitation of electrons (e$^-$) from the valence band to the conduction band takes place with simultaneous generation of the same number of holes in the valence band. Since the conduction band of ZTO-ZnO is −0.11 eV, which is lower than that of g-C$_3$N$_2$/ZTO-ZnO (−0.88 eV), the photoexcited electrons in the conduction band of g-C$_3$N$_2$/ZTO-ZnO can

easily be transferred to the conduction band of ZTO-ZnO. Therefore, the excited electrons on the conduction band of g-C$_3$N$_2$/ZTO-ZnO migrate to the conduction band of ZTO-ZnO as driven by the inner electric field between them. The valence band of ZTO-ZnO is +2.93 eV, which is higher than that of g-C$_3$N$_2$/ZTO-ZnO (+2.86 eV); consequently, the photoinduced holes in the valence band of ZTO-ZnO can be migrate to
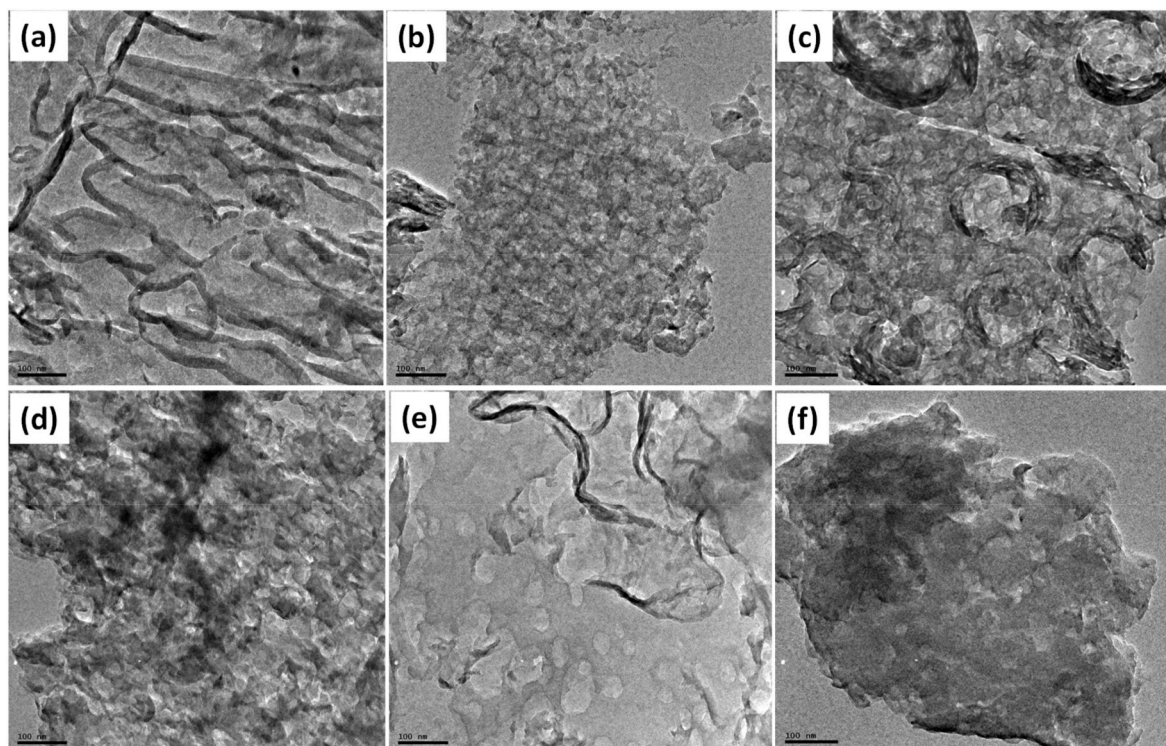
Fig. 8. TEM micrographs of (a) gC$_3$N$_4$, (b) gC$_3$N$_4$/ZTO-ZnO(2), (c) gC$_3$N$_4$/ZTO-ZnO(5), (d) gC$_3$N$_4$/ZTO-ZnO(10), (e) gC3N4/ZTO-ZnO(15), and (f) gC$_3$N$_4$/ZTO-ZnO(20).

the valence band of g-C$_3$N$_2$/ZTO-ZnO, resulting in an effective type II hetrojunction system of the ternary composite. There is an adequate separation of photogenerated electron-hole pairs at the heterojunction interfaces. This allows for the creation of more reactive species to participate in the photodegradation process. Thus, the electron in the conduction band of the ZTO-ZnO is capable of the reduction of the hexavalent chromium to its trivalent specie.

The synergistic effect of the nanosheet morphology and matching band structure between the semiconductors would contribute to enhanced photocatalytic activity of g-C$_3$N$_4$/ZnO/ZTO ternary composites [61]. After importing the surface oxygen vacancies on the composite, a few shallow surface oxygen vacancy states would emerge and partially overlap with the valence band maximum of the heterojunction. This could lead to the rising of the valence band maximum and the shrinking of band gap width [62] in the ternary heterojunction system.

3.7. Photoluminescence properties of the g-C$_3$N$_4$/ZTO-ZnO(20) heterojunction systems

Photoluminescence spectra of the ZTO-ZnO samples are shown in Fig. 12a, which was further used to explore the optical properties of the heterojunction systems. The spectra show the two major peaks in all the samples. The first peak in the UV region around 400 nm could be due to the excitonic emission caused by the Coulombic forces between electron-hole pairs, while the second peak observed around 800 nm occurs due to yellow-green defect emission, and could be attributed to the recombination between electrons and trapped holes [63].

The short peak which appears at 460 nm is the blue emission attributed to intrinsic defects such as zinc and oxygen interstitials. This peak which can only be observed for the ZTO-ZnO(10), ZTO-ZnO(15), and ZTO-ZnO(20) [64], suggests that the defects become more observable as the concentration of Sn ion was increased. The intensity decreased as the concentration of Sn ion increased. The ZTO-ZnO(20) exhibited the weakest PL intensity in all the samples, suggesting that it's the most efficient photocatalyst since it displayed the most efficient

restriction of recombination of photo-generated electron-hole pairs in the multi-component system.

The fluorescence spectrum of the composite of ZTO-ZnO and g-C$_3$N$_4$ show decreased PL intensity (Fig. 12b), which confirmed that the formation of heterojunction semiconductor materials resulted in the inhibition of electron-hole recombination, thus causing an increase in its photocatalytic activity [65,66]. The pristine g-C$_3$N$_4$ has an emission peak around 400 nm, which disappeared upon the formation of composite with the complex metal oxide nanoparticles, whilst aiding the inhibition of recombination process as evident in the reduction of the emission peak of the composite.

3.8. Photocatalytic studies

3.8.1. The effects of solution pH on the Cr(VI) reduction

The chemistry of Cr(VI) is pH dependent; thus, changes with the change in solution pH, which usually affects the removal or reduction of Cr(VI). This might be due to the changes that occur in the oxidation states while in solution and the charge densities of the photocatalysts. Therefore, 10 mg/L of Cr(VI) was investigated using ZTO-ZnO and g-C$_3$N$_4$/ZTO-ZnO(20) separately using the Cr(VI) dosage of 2 g/L, and the initial solution pH was varied from 2 to 8. At the initial stage, in both cases, the catalysts removed very small fraction of Cr(VI) in all pH range. However, increase in irradiation time increases the degradation rate of Cr(VI) to Cr(III) up to 120 min which is considered complete irradiation time with almost 100 % reduction rate (Fig. 12). Cr(VI) was gradually removed at the different time intervals using both ZTO-ZnO and g-C$_3$N$_4$/ZTO-ZnO(20) photocatalysts (Fig. 13 a and b). The highest removal of Cr (VI) at solution pH of 2, 4, 6, and 8 were 72 and 99.2 %; 50 and 85.6 %; 38 and 57.2 %; and 25 and 35 % for the ZTO-ZnO and g-C$_3$N$_4$/ZTO-ZnO (20) composites respectively.

The observed similarity in the reactions of these two different catalysts suggests that the photocatalytic removal of Cr(VI) increased with decrease in solution pH. This might be due to an increased potential difference between the conduction band of the catalysts and Cr(VI)/Cr
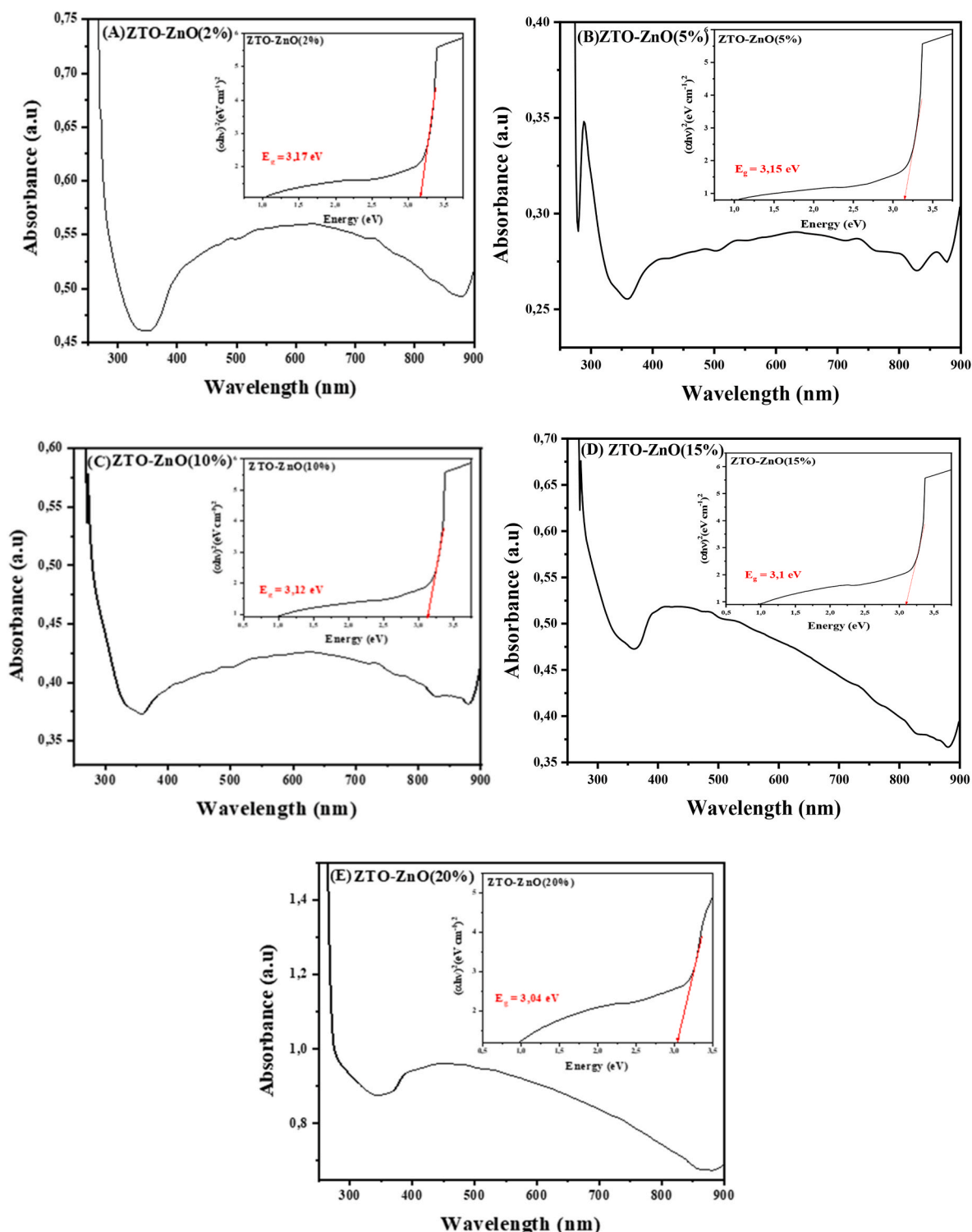
Fig. 9. Absorption spectra of (a) ZTO-ZnO(2), (b) ZTO-ZnO(5), (c) ZTO-ZnO(10), (d) ZTO-ZnO (15), and ZTO-ZnO(20), with their respective Tauc plot in the inset.

Table 3
Band gap energy of ZTO-ZnO nanoparticles.

Sample	Band gap energy (eV)
ZTO-ZnO(2)	3.17
ZTO-ZnO(5)	3.15
ZTO-ZnO(10)	3.12
ZTO-ZnO(15)	3.10
ZTO-ZnO(20)	3.04

(III) as well as the anionic-type adsorption of Cr(VI) on to the surface of both catalysts [67]. Also, the thermodynamic driving force for the reduction of Cr(VI) is related to the potential difference between the conduction band of the catalysts and the Cr(VI) ion [68]. The reduced removal rate observed at higher pH may also be attributed to the deposition of $Cr(OH)_3$ on the surface of the catalysts which could be ascribed to the adsorption of Cr(VI) on to the surface of catalysts and its subsequent redox reaction. Thus, photocatalytic reduction of Cr(VI) is possible either by direct capturing of photo-generated electrons or by
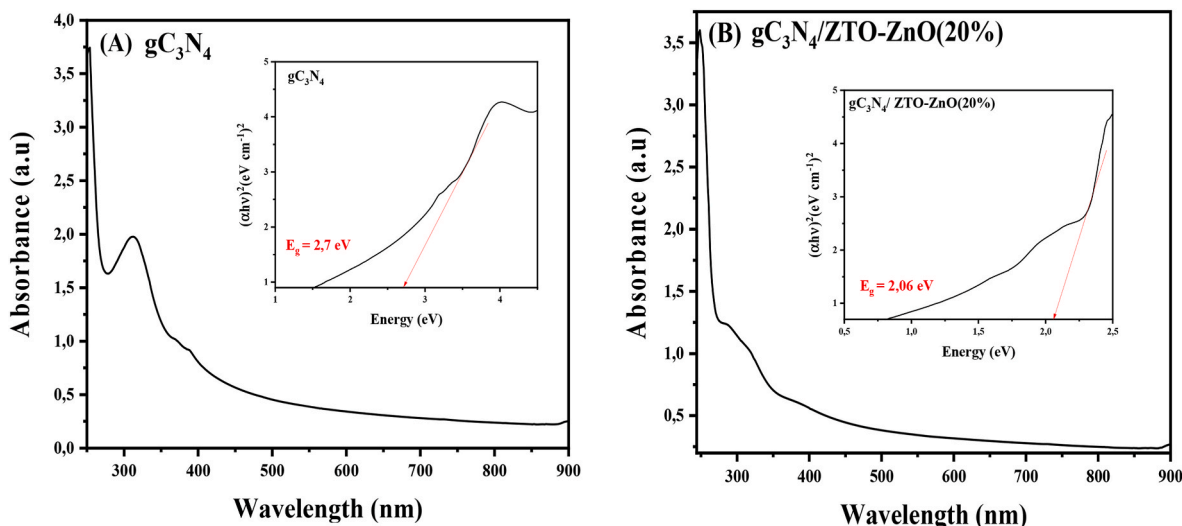
Fig. 10. Absorption spectra of (a) gC$_3$N$_4$, and (b) gC$_3$N$_4$/ZTO-ZnO(20). Insets are the respective Tauc plot obtained from a plot of $(\alpha h\nu)^2$ versus hν.

Table 4
First ionization energy, Electron affinity, and Mulliken's electronegativity of the nanoparticles.

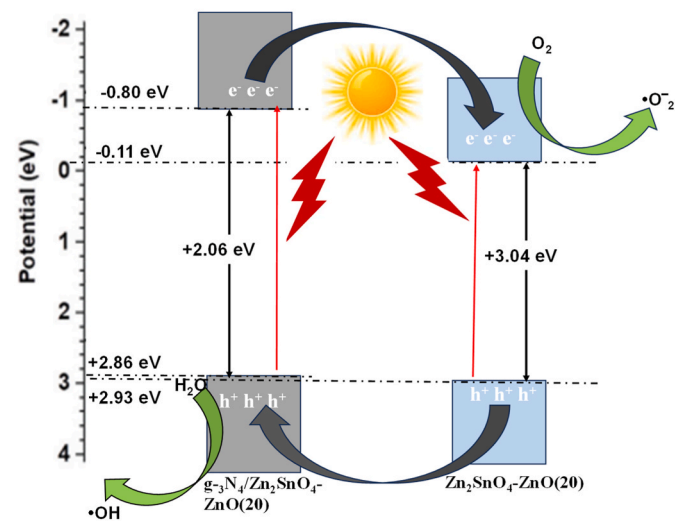| Element	First Ionization Energy eV)	Electron Affinity (eV)	$\chi_{element}$
Zinc	9.39	−0.6	4.397
Oxygen	13.62	1.46	7.539
Tin	7.34	1.11	4.226
Carbon	11.26	1.59	6.425
Nitrogen	14.53	0.07	7.300

Fig. 11. The energy band diagram of g-C$_3$N$_2$/ZTO-ZnO heterojunction nanoparticles showing the charge transportation processes.

indirect receiving of electrons from the surface of catalysts or even concurrently [68,69].

The speciation of Cr^{3+} depends on the solution pH, and hydrolysed Cr(OH)$_3$ is favoured at high solution pH [69]. The observed reduction efficiency obtained at pH 2 using g-C$_3$N$_4$/ZTO-ZnO(20) (Fig. 13a) was higher compared to ZTO-ZnO (Fig. 13b). Consequently, g-C$_3$N$_4$/ZTO-ZnO(20) was chosen for further Cr(VI) photocatalytic studies.
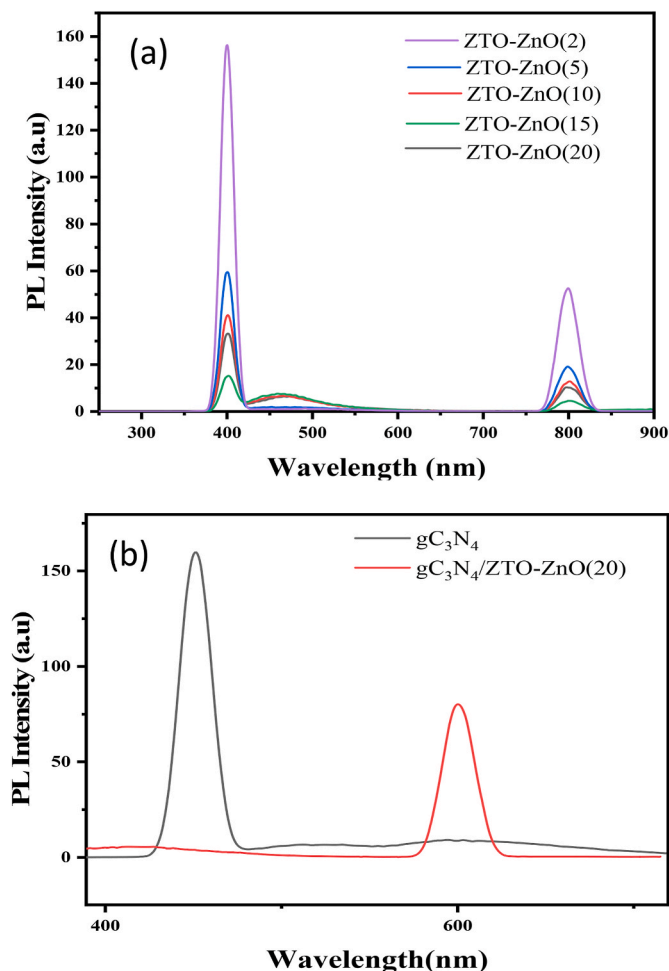

Fig. 12. Photoluminescence spectra of (a) ZTO-ZnO nanoparticles, (b) gC$_3$N$_4$ and gC$_3$N$_4$/ZTO-ZnO(20) nanocomposite.

3.8.2. Effect of photocatalyst (g-C$_3$N$_4$/ZTO-ZnO(20) dosage and initial concentration of Cr(IV) on the rate of reduction

Fig. 14a presents the effect of varying concentration (0.5–2 g) of g-C$_3$N$_4$/ZTO-ZnO(20) on the reduction of Cr(VI) to Cr(III) in aqueous solution. The removal rate of chromium increased with increase in the
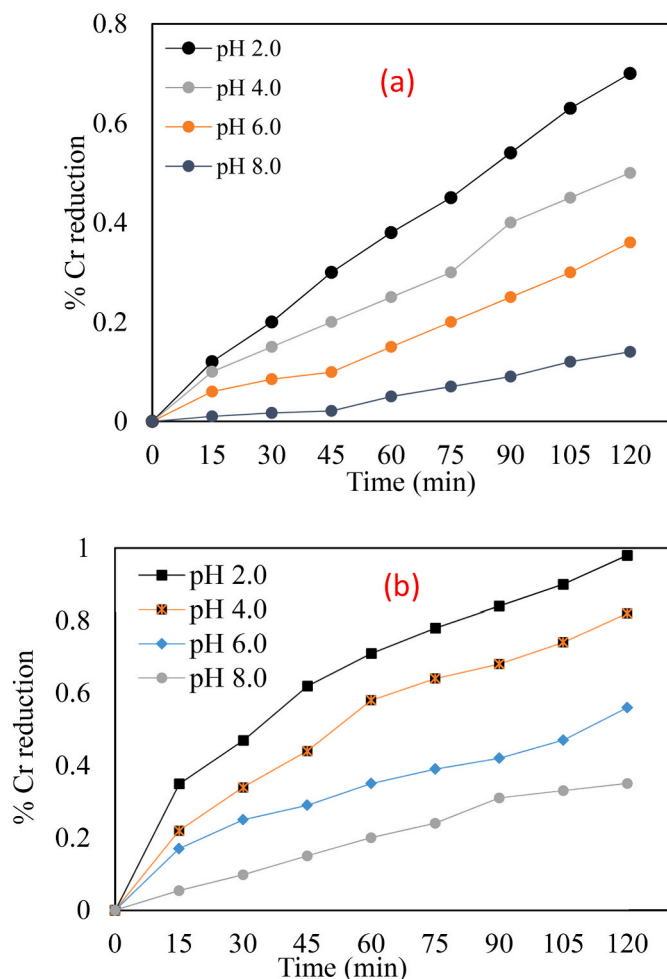
Fig. 13. Effect of solution pH on the reduction of Cr(VI) using (a) ZTO-ZnO(20) and (b) g-C$_3$N$_4$/ZTO-ZnO(20) (conc of photocatalyst = 2 g/L, Cr(VI) = 10 mg/L).

percentage of chromium removal also increased from 64 to 93.8 % at the optimum irradiation time.

The effect of initial concentrations of Cr(VI) was investigated within the range of 10–150 ppm, at an optimal conditions of pH 2 and 2 g/L of g-C$_3$N$_4$/ZTO-ZnO(20), and the results obtained are presented in Fig. 14b. It can be observed that an increase in initial Cr(VI) concentration increases the irradiation time required for complete degradation under the visible light. This observation could be rationalized according to Beer–Lambert's law: as Cr(VI) concentration increased, the path length of photons entering into the reaction mixture decreased, and only fewer photons could reach the catalyst's surface [70].

Therefore, the availability of active sites will be reduced, since the incident intensity, concentration of catalyst and irradiation time are constant. An increase in Cr(VI) concentrations could also lead to the exhaustion or the deactivation of accessible active sites on the photocatalyst, which could results in a reduction in the photo reduction rate [70,71].

3.8.3. Reusability studies

The possible industrial application of any synthesized or commercial photocatalyst is dependent on its reusability [72]. Therefore, the spent g-C$_3$N$_4$/ZTO-ZnO(20) was investigated for its reusability and photo stability to establish its robustness as a photocatalytic material. About 2 g/L of the prepared photocatalyst was used on a 10 mg/L of Cr(VI), and the result is presented in Fig. 15. Four cycles of recyclability studies was conducted, which shows that very small lost in the activity of the g-C$_3$N$_4$/ZTO-ZnO(20) occurred after four consecutive cycles. This indicates that it can be reused for up to four times. The activity of the nanocomposite decreases with the increase in the frequency of reuse, and this could be ascribed to the loss of the photocatalyst during the separation process. Similar observation has been reported in the previous studies [73,74] (see Table 5).

The high percentage reduction obtained with the g-C$_3$N$_4$/ZTO-ZnO (20) is comparable with the results reported for other g-C$_3$N$_4$ based composites in similar studies, which are presented in Table 6. The performance of the catalyst has economic value in water treatment as it implies that less photocatalyst will be needed to reduce Cr(VI) from water and this translates to cost efficiency.

The photocatalytic reaction kinetics of Cr(VI) is often modelled with the pseudo-first and second order kinetics models equation, which also cover the adsorption properties of the Cr(VI) on the photocatalyst surface. This model is expressed in equations (6) and (7).

catalyst dosage. Consequently, the highest chromium removal percentage was found to be 99.2 % at photocatalyst loading of 2 g/L. As the g-C$_3$N$_4$/ZTO-ZnO(20) loading was increased from 0.5 to 2 g/L, the
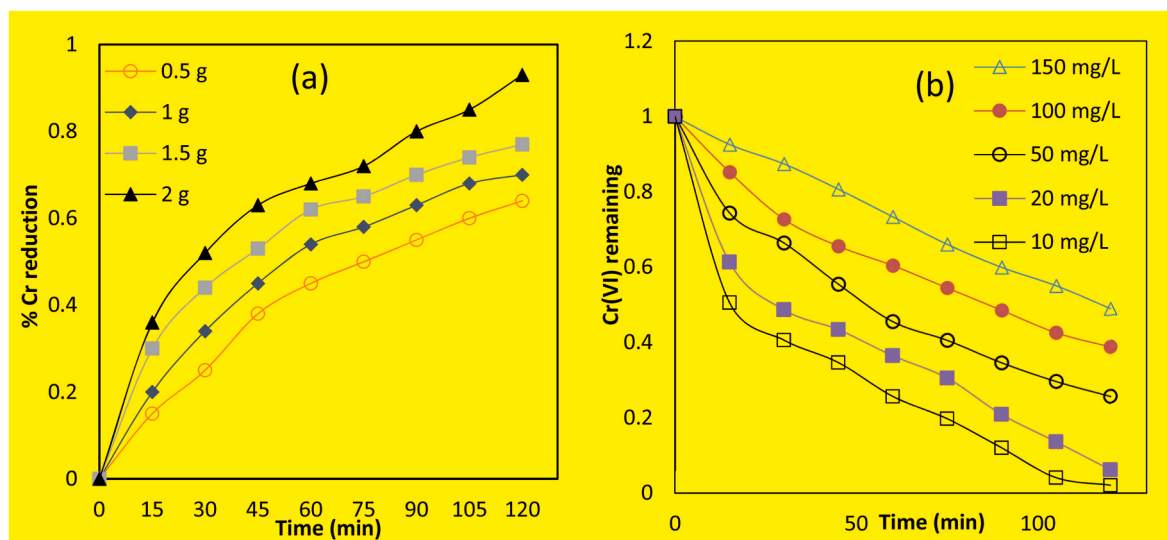

Fig. 14. The effect of (a) catalyst loading, and (b) Cr(VI) concentration on the photoreduction process using g-C$_3$N$_4$/ZTO-ZnO(20), (dosage: 2 g/L, irradiation time: 120 min, pH: 2).
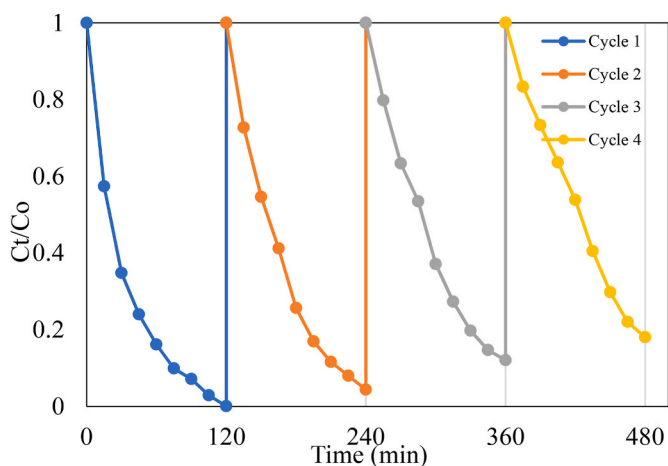
Fig. 15. Reusability cycles of Cr(VI) reduction using g-C$_3$N$_4$/ZTO-ZnO(20) nanocomposite and a solution of 10 mg/L Cr(IV).

Fig. 16. (a) Pseudo first order model for Cr(VI) photo degradation by g-C$_3$N$_4$/ZTO-ZnO(20) (dosage: 2 g/L, irradiation time: 120 min, pH: 2).

Table 5
Mulliken's electronegativity, band gap energy, conduction band, and valence band of the pristine graphitic carbon nitride and the nanocomposite.

Semiconductors	Mulliken's electronegativity (eV)	Bandgap energy (eV)	Conduction band potential (eV)	Valence band potential (eV)
gC$_3$N$_4$	4.22	2.70	−1.63	+1.07
Zn$_2$SnO$_4$–ZnO (20)	5.91	3.04	−0.11	+2.93
g-$_3$N$_4$/ Zn$_2$SnO$_4$– ZnO (20)	6.33	2.06	−0.80	+2.86

Table 6
Comparison of photocatalytic reduction values obtained from g-C$_3$N$_4$/Zn$_2$SnO$_4$–ZnO nanocomposite with the percentage Cr(VI) reduction of different g-C$_3$N$_4$ base nanocomposite in reported studies.

Photocatalysts	pollutant treated	%reduction	References
g-C$_3$N$_4$/Zn$_2$SnO$_4$–ZnO	Cr(VI)	99.2	This study
AgNP/Eg-C$_3$N$_4$/CS	Cr(VI)	98.5	[75]
(g-C$_3$N$_4$/NH$_2$-MIL-101(Fe)	Cr(VI)	91	[76]
Co$_9$S$_8$/g-C$_3$N$_4$)	Cr(VI)	81	[77]
2D/2D SnS$_2$/g-C$_3$N$_4$	Cr(VI)	99	[78]
Zn$_2$SnO$_4$–ZnO Nanocomposite	Cr(VI)	72	This study

Thus, the pseudo-first and second order, kinetics model equations can be expressed in equations (6) and (7) respectively:

$$\log(q_e - q_t) = \log q_e - \frac{k_1}{2.303}t \qquad (6)$$

$$\frac{t}{q_t} = \frac{1}{k_2 q_e} + \frac{1}{q_e}t \qquad (7)$$

where.

q_e is the degradation capacity (mg/g) of solute at equilibrium

q_t are the degradation capacity (mg/g) of solute at time t (min), k_1 (min^{-1}) and k_2 (g/mg·min) are both rate constants of the pseudo-first and pseudo-second order respectively.

The results obtained by comparing their correlation coefficient (R^2) values (Fig. 16) suggested that pseudo-first order model well described the photocatalytic activity of g-C$_3$N$_4$/ZTO-ZnO(20) on the reduction of Cr(VI) to Cr(III) compared to pseudo-second order kinetics model. The reaction rate constants (k) for the photocatalytic reduction of Cr(VI) were evaluated from experimental data using the linear regression
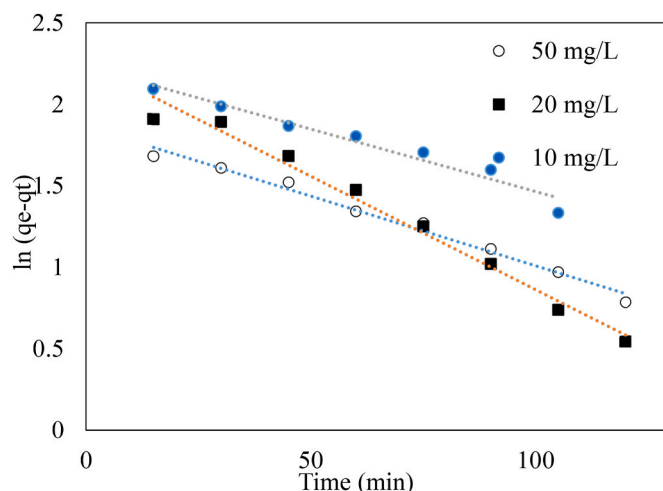
analysis method. The constants k_1 and k_2 (first and second order reaction rate constants) were obtained as 19.6 and 1.4 g/mg.min respectively (Table 7). A non-linear regression method was used to calculate the best values of model constants. A high correlation coefficient ($R^2 = 0.999$) confirms the validity of the pseudo-first order model. This is an indication that the photoreduction of Cr(VI) occurred mainly on the surface of the catalyst and the photoreduction step is the limited step and also determines the overall reaction rate [79]. Also, the increase in overall rate constant k with an increase in initial Cr(VI) concentration could be due to the mass transfer limitations at high concentrations. These results were similar to earlier reported studies [80,81].

4. Conclusion

In conclusion, the application of ternary heterojunction composite (g-C$_3$N$_4$/ZTO-ZnO) for visible light enhanced photocatalytic reduction of Cr(VI) to Cr(III) in aqueous solutions was studied. The prepared composites were characterized by XRD, SEM, TEM EDX and UV–visible spectroscopy. The photocatalytic assessment indicated that the ternary composite exhibited superior reduction efficiency of Cr(VI) (99.2%) compared to the binary composite (72%) at pH 2. As the pH increased from 2 to 8, the reduction efficiency decreased. An increase in the catalyst dosage was found to be directly proportional to the reduction to Cr(III), while an increase in the concentration of Cr(VI) impeded the removal process. The matched energy band structure of the heterostructure semiconductors promoted carrier migration and visible light absorption. However, the photocatalytic performance of g-C$_3$N$_4$/ZTO-ZnO heterojunction for Cr (VI) reduction was much higher than that of pristine ZTO-ZnO. The large specific surface area of the graphitic carbon nitride, its porous nature, and reduction of recombination process was responsible for the enhanced efficiency of the graphitic carbon nitride containing ternary composite compared to the pristine complex metal oxide (ZTO-ZnO). Kinetic studies showed that the photoreduction of Cr

Table 7
Kinetics parameters for Cr onto g-C$_3$N$_4$/ZTO-ZnO(20) photocatalysts.

Co (mg/L)	Pseudo-first-order model parameter			Pseudo-second-order model parameter		
	k$_1$ x10^{-2} (g/mg.min)	a (mg/g)	R^2	q$_e$ (mg/g)	k$_2$ 10^{-2} (g/mg.min)	R^2
10	1.77	9.53	0.995	14.5	5.1	0.787
20	3.20	9.51	0.998	17.2	3.6	0.765
50	19.6	6.46	0.988	13.1	1.4	0.697

(VI) was well-fitted to pseudo-first order model. This is an indication that the photoreduction of Cr(VI) occurred mainly on the surface of the catalyst and the photoreduction step is the limited step and also determines the overall reaction rate.

Declaration of competing interest

The authors declare that they have no known competing financial interests or personal relationships that could have appeared to influence the work reported in this paper

Data availability

Data will be made available on request.

Acknowledgments

References

[1] M. Qamar, M. Gondal, Z. Yamani, Laser-induced efficient reduction of Cr (VI) catalyzed by ZnO nanoparticles, J. Hazard Mater. 187 (2011) 258–263.

[2] J.A. Jacobs, S.M. Testa, Overview of chromium (VI) in the environment: background and history, Chromium (VI) handbook (2005) 1–21.

[3] E. Vaiopoulou, P. Gikas, Regulations for chromium emissions to the aquatic environment in Europe and elsewhere, Chemosphere 254 (2020), 126876.

[4] A. Elahi, I. Arooj, D.A. Bukhari, A. Rehman, Successive use of microorganisms to remove chromium from wastewater, Appl. Microbiol. Biotechnol. 104 (2020) 3729–3743.

[5] T.O. Ajiboye, O.A. Oyewo, D.C. Onwudiwe, Conventional and current methods of toxic metals removal from water using g-C3N4-based materials, J. Inorg. Organomet. Polym. Mater. 31 (2021) 1419–1442.

[6] D.E. Kimbrough, Y. Cohen, A.M. Winer, L. Creelman, C. Mabuni, A critical assessment of chromium in the environment, Crit. Rev. Environ. Sci. Technol. 29 (1999) 1–46.

[7] T.A. Khan, M. Nazir, I. Ali, A. Kumar, Removal of chromium (VI) from aqueous solution using guar gum–nano zinc oxide biocomposite adsorbent, Arab. J. Chem. 10 (2017) S2388–S2398.

[8] M. Deravanesiyan, M. Beheshti, A. Malekpour, The removal of Cr (III) and Co (II) ions from aqueous solution by two mechanisms using a new sorbent (alumina nanoparticles immobilized zeolite)—equilibrium, kinetic and thermodynamic studies, J. Mol. Liq. 209 (2015) 246–257.

[9] M. Dakiky, M. Khamis, A. Manassra, M. Mer'Eb, Selective adsorption of chromium (VI) in industrial wastewater using low-cost abundantly available adsorbents, Adv. Environ. Res. 6 (2002) 533–540.

[10] M. Ismael, Structure, properties, and characterization of mullite-type materials Bi2M4O9 and their applications in photocatalysis: a review, J. Environ. Chem. Eng. (2022), 108640.

[11] H. Karimi-Maleh, Y. Orooji, A. Ayati, S. Qanbari, B. Tanhaei, F. Karimi, M. Alizadeh, J. Rouhi, L. Fu, M. Sillanpää, Recent advances in removal techniques of Cr (VI) toxic ion from aqueous solution: a comprehensive review, J. Mol. Liq. (2020), 115062.

[12] M. Ismael, Environmental remediation and sustainable energy generation via photocatalytic technology using rare earth metals modified g-C3N4: a review, J. Alloys Compd. (2022), 167469.

[13] J. Ge, Y. Zhang, Y.-J. Heo, S.-J. Park, Advanced design and synthesis of composite photocatalysts for the remediation of wastewater: a review, Catalysts 9 (2019) 122.

[14] S. Baruah, J. Dutta, Zinc stannate nanostructures: hydrothermal synthesis, Sci. Technol. Adv. Mater. 12 (2011), 1-N.PAG.

[15] S. Sun, S. Liang, Morphological zinc stannate: synthesis, fundamental properties and applications, J. Mater. Chem. A 5 (2017) 20534–20560.

[16] J. Xu, X. Jia, X. Lou, J. Shen, One-step hydrothermal synthesis and gas sensing property of ZnSnO3 microparticles, Solid State Electron. 50 (2006) 504–507.

[17] M. Miyauchi, Z. Liu, Z.-G. Zhao, S. Anandan, K. Hara, Single crystalline zinc stannate nanoparticles for efficient photo-electrochemical devices, Chem. Commun. 46 (2010) 1529–1531.

[18] T. Tangcharoen, C. Kongmark, W. Pecharapa, Synchrotron X-ray absorption spectroscopy study of the local atomic structures and cation ordering in perovskite- and spinel-type zinc stannate synthesized by co-precipitation method, J. Mol. Struct. 1102 (2015) 95–100.

[19] D. Kovacheva, K. Petrov, Preparation of crystalline ZnSnO3 from Li2SnO3 by low-temperature ion exchange, Solid State Ionics 109 (1998) 327–332.

[20] H. Gou, J. Zhang, Z. Li, G. Wang, F. Gao, R.C. Ewing, J. Lian, Energetic stability, structural transition, and thermodynamic properties of ZnSnO 3, Appl. Phys. Lett. 98 (2011), 091914.

[21] M.-K. Lo, S.-Y. Lee, K.-S. Chang, Study of ZnSnO3-nanowire piezophotocatalyst using two-step hydrothermal synthesis, J. Phys. Chem. C 119 (2015) 5218–5224.

[22] E.L. Foletto, J.M. Simões, M.A. Mazutti, S.L. Jahn, E.I. Muller, L.S.F. Pereira, E. M. de Moraes Flores, Application of Zn2SnO4 photocatalyst prepared by microwave-assisted hydrothermal route in the degradation of organic pollutant under sunlight, Ceram. Int. 39 (2013) 4569–4574.

[23] D. An, Q. Wang, X. Tong, Q. Zhou, Z. Li, Y. Zou, X. Lian, Y. Li, Synthesis of Zn2SnO4 via a co-precipitation method and its gas-sensing property toward ethanol, Sensor. Actuator. B Chem. 213 (2015) 155–163.

[24] B. Ayesha, U. Jabeen, A. Naeem, P. Kasi, M.N.K. Malghani, S.U. Khan, J. Akhtar, M. Aamir, Synthesis of zinc stannate nanoparticles by sol-gel method for photocatalysis of commercial dyes, Results in Chemistry 2 (2020), 100023.

[25] M.M. Jaculine, C.J. Raj, S.J. Das, Hydrothermal synthesis of highly crystalline Zn2SnO4 nanoflowers and their optical properties, J. Alloys Compd. 577 (2013) 131–137.

[26] A.A. Firooz, A.R. Mahjoub, A.A. Khodadadi, M. Movahedi, High photocatalytic activity of Zn2SnO4 among various nanostructures of Zn2xSn1− xO2 prepared by a hydrothermal method, Chem. Eng. J. 165 (2010) 735–739.

[27] A. Pandimurugan, K. Sankaranarayanan, Antibacterial and photocatalytic activity of ZnO, SnO2 and Zn2SnO4 nanoparticles prepared by Microwave assisted method, Mater. Technol. (2021) 1–11.

[28] D. Lei, J. Xue, Q. Bi, C. Tang, L. Zhang, 3D/2D direct Z-scheme photocatalyst Zn2SnO4/CdS for simultaneous removal of Cr (VI) and organic pollutant, Appl. Surf. Sci. 517 (2020), 146030.

[29] S. Dong, L. Cui, Y. Tian, L. Xia, Y. Wu, J. Yu, D.M. Bagley, J. Sun, M. Fan, A novel and high-performance double Z-scheme photocatalyst ZnO-SnO2-Zn2SnO4 for effective removal of the biological toxicity of antibiotics, J. Hazard Mater. 399 (2020), 123017.

[30] N. Rono, J.K. Kibet, B.S. Martincigh, V.O. Nyamori, A review of the current status of graphitic carbon nitride, Crit. Rev. Solid State Mater. Sci. 46 (2021) 189–217.

[31] G. Dong, L. Zhang, Porous structure dependent photoreactivity of graphitic carbon nitride under visible light, J. Mater. Chem. 22 (2012) 1160–1166.

[32] M. Ismael, A review on graphitic carbon nitride (g-C3N4) based nanocomposites: synthesis, categories, and their application in photocatalysis, J. Alloys Compd. 846 (2020), 156446.

[33] M. Ismael, Facile synthesis of NiO-loaded g-C3N4 heterojunction photocatalyst for efficient photocatalytic degradation of 4-nitrophenol under visible light irradiation, J. Photochem. Photobiol. Chem. 439 (2023), 114576.

[34] M. Ismael, One-step ultrasonic-assisted synthesis of Ni-doped g-C3N4 photocatalyst for enhanced photocatalytic hydrogen evolution, Inorg. Chem. Commun. 151 (2023), 110607.

[35] M. Ismael, M. Wark, Photocatalytic activity of CoFe2O4/g-C3N4 nanocomposite toward degradation of different organic pollutants and their inactivity toward hydrogen production: the role of the conduction band position, FlatChem 32 (2022), 100337.

[36] D.C. Onwudiwe, P.A. Ajibade, Synthesis and characterization of metal complexes of N-alkyl-N-phenyl dithiocarbamates, Polyhedron 29 (2010) 1431–1436.

[37] M. Ben Ali, F. Barka-Bouaifel, H. Elhouichet, B. Sieber, A. Addad, L. Boussekey, M. Férid, R. Boukherroub, Hydrothermal synthesis, phase structure, optical and photocatalytic properties of Zn2SnO4 nanoparticles, J. Colloid Interface Sci. 457 (2015) 360–369.

[38] S. Vinoth, P. Mary Rajaitha, A. Pandikumar, In-situ Pyrolytic Processed Zinc Stannate Incorporated Graphitic Carbon Nitride Nanocomposite for Selective and Sensitive Electrochemical Determination of Nitrobenzene, Composites Science & Technology, 2020, p. 195. N.PAG-N.PAG.

[39] S. Vinoth, R. Ramaraj, A. Pandikumar, Facile synthesis of calcium stannate incorporated graphitic carbon nitride nanohybrid materials: a sensitive electrochemical sensor for determining dopamine, Mater. Chem. Phys. (2020) 245. N.PAG-N.PAG.

[40] J.E. Jeronsia, L.A. Joseph, M.M. Jaculine, P.A. Vinosha, S.J. Das, Hydrothermal synthesis of zinc stannate nanoparticles for antibacterial applications, J. Taibah Univ. Sci. 10 (2016) 601–606.

[41] T. Fang, X. Yang, L. Zhang, J. Gong, Ultrasensitive photoelectrochemical determination of chromium(VI) in water samples by ion-imprinted/formate anion-incorporated graphitic carbon nitride nanostructured hybrid, J. Hazard Mater. 312 (2016) 106–113.

[42] D. Venkappayya, THERMAL DECOMPOSITION OF THE COMPLEXES OF DITHIOCARBAMATE AND SUBSTITUTED THIOUREA WITH NI (II), ZN (II), CD (II), CR (III) AND CO (III), 1974.

[43] J.O. Hill, J.P. Murray, K.C. Patil, The thermochemistry of the metal dithiocarbamate and xanthate complexes - a review up-date, Rev. Inorg. Chem. 14 (1994) 363–387.

[44] D. Onwudiwe, A. Ekennia, Synthesis, characterization, thermal, antimicrobial and antioxidant studies of some transition metal dithiocarbamates, Res. Chem. Intermed. 43 (2017) 1465–1485.

[45] A.K. Sharma, Thermal behaviour of metal-dithiocarbamates, Thermochim. Acta 104 (1986) 339–372.

[46] K.J. Cavell, J.O. Hill, R.J. Magee, Standard enthalpy of formation of bis (diethyldithiocarbamato) copper (II) at 298 K and the copper–sulphur bond energy, J. Chem. Soc., Dalton Trans. (1980) 1638–1640.

[47] S.T. Breviglieri, E.T. Cavalheiro, G.O. Chierice, Correlation between ionic radius and thermal decomposition of Fe(II), Co(II), Ni(II), Cu(II) and Zn(II) diethanoldithiocarbamates, Thermochim. Acta 356 (2000) 79–84.

[48] B. Macias, J. Criado, M. Vaquero, M. Villa, Thermal stability of dithiocarbamates derived from α-amino acids with different metal ions, Thermochim. Acta 223 (1993) 213–221.

[49] R. Pike, H. Cui, R. Kershaw, K. Dwight, A. Wold, T. Blanton, A. Wernberg, H. Gysling, Preparation of zinc sulfide thin films by ultrasonic spray pyrolsis from bis (diethyldithiocarbamato) zinc (II), Thin Solid Films 224 (1993) 221–226.

[50] S. Baruah, S.S. Sinha, B. Ghosh, S.K. Pal, A. Raychaudhuri, J. Dutta, Photoreactivity of ZnO nanoparticles in visible light: effect of surface states on electron transfer reaction, J. Appl. Phys. 105 (2009), 074308.

[51] S. Danwittayakul, M. Jaisai, J. Dutta, Efficient solar photocatalytic degradation of textile wastewater using ZnO/ZTO composites, Appl. Catal. B Environ. 163 (2015) 1–8.

[52] S. Danwittayakul, M. Jaisai, T. Koottatep, J. Dutta, Enhancement of photocatalytic degradation of methyl orange by supported zinc oxide nanorods/zinc stannate (ZnO/ZTO) on porous substrates, Ind. Eng. Chem. Res. 52 (2013) 13629–13636.

[53] Q. Lin, Z. Li, T. Lin, B. Li, X. Liao, H. Yu, C. Yu, Controlled preparation of P-doped g-C3N4 nanosheets for efficient photocatalytic hydrogen production, Chin. J. Chem. Eng. 28 (2020) 2677–2688.

[54] R. Hao, G. Wang, C. Jiang, H. Tang, Q. Xu, In situ hydrothermal synthesis of g-C3N4/TiO2 heterojunction photocatalysts with high specific surface area for Rhodamine B degradation, Appl. Surf. Sci. 411 (2017) 400–410.

[55] A. Raza, H. Shen, A.A. Haidry, Novel Cu2ZnSnS4/Pt/g-C3N4 heterojunction photocatalyst with straddling band configuration for enhanced solar to fuel conversion, Appl. Catal. B Environ. 277 (2020), 119239.

[56] S. Panimalar, R. Uthrakumar, E.T. Selvi, P. Gomathy, C. Inmozhi, K. Kaviyarasu, J. Kennedy, Studies of MnO2/g-C3N4 hetrostructure efficient of visible light photocatalyst for pollutants degradation by sol-gel technique, Surface. Interfac. 20 (2020), 100512.

[57] R.C. Ngullie, S.O. Alaswad, K. Bhuvaneswari, P. Shanmugam, T. Pazhanivel, P. Arunachalam, Synthesis and characterization of efficient ZnO/g-C3N4 nanocomposites photocatalyst for photocatalytic degradation of methylene blue, Coatings 10 (2020) 500.

[58] S. Li, Z. Ma, J. Zhang, Y. Wu, Y. Gong, A comparative study of photocatalytic degradation of phenol of TiO2 and ZnO in the presence of manganese dioxides, Catal. Today 139 (2008) 109–112.

[59] H. Che, C. Li, P. Zhou, C. Liu, H. Dong, C. Li, Band structure engineering and efficient injection rich-π-electrons into ultrathin g-C3N4 for boosting photocatalytic H2-production, Appl. Surf. Sci. 505 (2020), 144564.

[60] M. Mousavi, A. Habibi-Yangjeh, M. Abitorabi, Fabrication of novel magnetically separable nanocomposites using graphitic carbon nitride, silver phosphate and silver chloride and their applications in photocatalytic removal of different pollutants using visible-light irradiation, J. Colloid Interface Sci. 480 (2016) 218–231.

[61] Y. Yuan, G.-F. Huang, W.-Y. Hu, D.-N. Xiong, B.-X. Zhou, S. Chang, W.-Q. Huang, Construction of g-C3N4/CeO2/ZnO ternary photocatalysts with enhanced photocatalytic performance, J. Phys. Chem. Solid. 106 (2017) 1–9.

[62] D. Chen, S. Wu, J. Fang, S. Lu, G. Zhou, W. Feng, F. Yang, Y. Chen, Z. Fang, A nanosheet-like α-Bi2O3/g-C3N4 heterostructure modified by plasmonic metallic Bi and oxygen vacancies with high photodegradation activity of organic pollutants, Sep. Purif. Technol. 193 (2018) 232–241.

[63] C. Tuc Altaf, N.S. Sahsuvar, N. Abdullayeva, O. Coskun, A. Kumtepe, E. Karagoz, M. Sankir, N. Demirci Sankir, Inverted configuration of Cu (in, Ga) S2/in2S3 on 3D-ZnO/ZnSnO3 bilayer system for highly efficient photoelectrochemical water splitting, ACS Sustain. Chem. Eng. 8 (2020) 15209–15222.

[64] S. Bhatia, N. Verma, R. Bedi, Sn-doped ZnO nanopetal networks for efficient photocatalytic degradation of dye and gas sensing applications, Appl. Surf. Sci. 407 (2017) 495–502.

[65] S. Ghattavi, A. Nezamzadeh-Ejhieh, A visible light driven AgBr/g-C3N4 photocatalyst composite in methyl orange photodegradation: focus on photoluminescence, mole ratio, synthesis method of g-C3N4 and scavengers, Compos. B Eng. 183 (2020), 107712.

[66] S. Wu, H.-J. Zhao, C.-F. Li, J. Liu, W. Dong, H. Zhao, C. Wang, Y. Liu, Z.-Y. Hu, L. Chen, Type II heterojunction in hierarchically porous zinc oxide/graphitic carbon nitride microspheres promoting photocatalytic activity, J. Colloid Interface Sci. 538 (2019) 99–107.

[67] P. Sane, S. Chaudhari, P. Nemade, S. Sontakke, Photocatalytic reduction of chromium (VI) using combustion synthesized TiO2, J. Environ. Chem. Eng. 6 (2018) 68–73.

[68] Q. Cheng, C. Wang, K. Doudrick, C.K. Chan, Hexavalent chromium removal using metal oxide photocatalysts, Appl. Catal. B Environ. 176–177 (2015) 740–748.

[69] A. Idris, N. Hassan, N.S. Mohd Ismail, E. Misran, N.M. Yusof, A.-F. Ngomsik, A. Bee, Photocatalytic magnetic separable beads for chromium (VI) reduction, Water Res. 44 (2010) 1683–1688.

[70] T.N. Ravishankar, M.d.O. Vaz, T. Ramakrishnappa, S.R. Teixeira, J. Dupont, Ionic liquid assisted hydrothermal syntheses of Au doped TiO2 NPs for efficient visible-light photocatalytic hydrogen production from water, electrochemical detection and photochemical detoxification of hexavalent chromium (Cr6+), RSC Adv. 7 (2017) 43233–43244.

[71] J.J. Testa, M.A. Grela, M.I. Litter, Heterogeneous photocatalytic reduction of chromium(VI) over TiO2 particles in the presence of oxalate: involvement of Cr(V) species, Environ. Sci. Technol. 38 (2004) 1589–1594.

[72] A. Balakrishnan, M. Chinthala, Comprehensive review on advanced reusability of g-C3N4 based photocatalysts for the removal of organic pollutants, Chemosphere 297 (2022), 134190.

[73] D.H. Quiñones, A. Rey, P.M. Álvarez, F.J. Beltrán, P.K. Plucinski, Enhanced activity and reusability of TiO2 loaded magnetic activated carbon for solar photocatalytic ozonation, Appl. Catal. B Environ. 144 (2014) 96–106.

[74] Y. Liu, C. Bian, Y. Li, P. Sun, Y. Xiao, X. Xiao, W. Wang, X. Dong, Aminobenzaldehyde convelently modified graphitic carbon nitride photocatalyst through Schiff base reaction: regulating electronic structure and improving visible-light-driven photocatalytic activity for moxifloxacin degradation, J. Colloid Interface Sci. 630 (2023) 867–878.

[75] E. Prabakaran, K. Pillay, Self-assembled silver nanoparticles decorated on exfoliated graphitic carbon nitride/carbon sphere nanocomposites as a novel catalyst for catalytic reduction of Cr(VI) to Cr(III) from wastewater and reuse for photocatalytic applications, ACS Omega 6 (2021) 35221–35243.

[76] D. Pattappan, K.V. Kavya, S. Vargheese, R.T.R. Kumar, Y. Haldorai, Graphitic carbon nitride/NH2-MIL-101(Fe) composite for environmental remediation: visible-light-assisted photocatalytic degradation of acetaminophen and reduction of hexavalent chromium, Chemosphere 286 (2022), 131875.

[77] J. Gu, H. Chen, F. Jiang, X. Wang, L. Li, All-solid-state Z-scheme Co9S8/graphitic carbon nitride photocatalysts for simultaneous reduction of Cr(VI) and oxidation of 2,4-dichlorophenoxyacetic acid under simulated solar irradiation, Chem. Eng. J. 360 (2019) 1188–1198.

[78] E.D. Koutsouroubi, I. Vamvasakis, C. Drivas, S. Kennou, G.S. Armatas, Photochemical deposition of SnS2 on graphitic carbon nitride for photocatalytic aqueous Cr(VI) reduction, Chemical Engineering Journal Advances 9 (2022), 100224.

[79] M.A. Behnajady, N. Mansoriieh, N. Modirshahla, M. Shokri, Influence of operational parameters and kinetics analysis on the photocatalytic reduction of Cr (VI) by immobilized ZnO, Environ. Technol. 33 (2012) 265–271.

[80] G.H. Safari, M. Hoseini, M. Seyedsalehi, H. Kamani, J. Jaafari, A.H. Mahvi, Photocatalytic degradation of tetracycline using nanosized titanium dioxide in aqueous solution, Int. J. Environ. Sci. Technol. 12 (2015) 603–616.

[81] H.O.N. Stancl, K. Hristovski, P. Westerhoff, Hexavalent chromium removal using UV-TiO2/ceramic membrane reactor, Environ. Eng. Sci. 32 (2015) 676–683.